

# Observational Constraints on the Physical Properties of Interstellar Dust in the Post-Planck Era

Brandon S. Hensley and B. T. Draine

Department of Astrophysical Sciences, Princeton University, Princeton, NJ 08544, USA; bhensley@astro.princeton.edu Received 2020 August 28; revised 2020 October 26; accepted 2020 October 27; published 2021 January 11

### **Abstract**

We present a synthesis of the astronomical observations constraining the wavelength-dependent extinction, emission, and polarization from interstellar dust from UV to microwave wavelengths on diffuse Galactic sight lines. Representative solid-phase abundances for those sight lines are also derived. Given the sensitive new observations of polarized dust emission provided by the Planck satellite, we place particular emphasis on dust polarimetry, including continuum polarized extinction, polarization in the carbonaceous and silicate spectroscopic features, the wavelength-dependent polarization fraction of the dust emission, and the connection between optical polarized extinction and far-infrared polarized emission. Together, these constitute a set of constraints that should be reproduced by models of dust in the diffuse interstellar medium.

*Unified Astronomy Thesaurus concepts:* Dust continuum emission (412); Interstellar dust (836); Interstellar dust extinction (837); Starlight polarization (1571); Polycyclic aromatic hydrocarbons (1280); Silicate grains (1456); Interstellar scattering (854)

Supporting material: data behind figure

#### 1. Introduction

Interstellar dust is manifest at nearly all wavelengths of astronomical interest, scattering, absorbing, and emitting radiation from X-ray to radio wavelengths. Embedded in this diversity of phenomena are clues to the nature of interstellar grains—their size, shape, composition, and optical properties.

A combination of astronomical observations, laboratory studies, and theoretical calculations has informed a picture of interstellar dust that consists of, at minimum, amorphous silicate and carbonaceous materials (see Draine 2003a for a review). However, many questions remain as to the details of these components, e.g., their optical properties, porosity, purity, size distributions, shapes, and alignment, including whether the silicate and carbonaceous materials exist as distinct components or whether they are typically found in the same interstellar grains.

The astronomical data that constrain models of interstellar dust are extensive and ever increasing in detail. Determinations of solid-phase abundances define the elemental makeup and mass of interstellar dust grains per H atom. Interstellar extinction has been measured from the far-UV (FUV) through the mid-infrared (MIR), including a number of spectral features suggesting specific materials. Emission from dust grains heated by the ambient interstellar radiation field has been observed from the near-infrared (NIR) through the microwave. Additionally, anomalous microwave emission (AME), thought to arise from rapidly rotating ultrasmall grains, is seen at radio frequencies while extended red emission (ERE), attributed to fluorescence, is observed in the optical. Polarization has been detected in both extinction and emission, including in some spectral features, placing additional constraints on the shapes, compositions, and alignment properties of interstellar grains.

With high-sensitivity far-infrared (FIR) imaging and polarimetry, the Planck satellite measured the properties of submillimeter polarized dust emission in unprecedented detail (Planck Collaboration Int. XIX 2015). The very high

<sup>1</sup> Spitzer Fellow.

submillimeter polarization fractions and the observed characteristic ratios between polarized FIR emission and polarized extinction at optical wavelengths have posed serious challenges to pre-Planck dust models (Planck Collaboration Int. XIX 2015; Planck Collaboration XII 2020). It is imperative that these new findings guide the development of the next generation of models.

When presenting a new dust model, it has become customary to detail the set of observations that constrain it (e.g., Mathis et al. 1977; Draine & Lee 1984; Zubko et al. 2004; Draine & Fraisse 2009; Compiègne et al. 2011; Siebenmorgen et al. 2014; Guillet et al. 2018). Given the now vast array of observations that can be employed in calibrating and testing models, and given also the heterogeneity of the observations in terms of wavelengths covered and region observed, synthesizing a coherent set of model constraints can be as challenging as constructing the model itself. Sight line to sight line variations exist, and we can aim only to identify observational constraints that appear to be representative of characteristic environments. It is therefore the goal of this work to summarize the current state of observations constraining the properties of dust in the diffuse interstellar medium (ISM) and to establish a set of benchmark constraints against which models of interstellar dust can be tested. We focus here on diffuse atomic sight lines where the observational constraints are most complete. As such, the properties of dust in dense clouds, such as ice features, will not be discussed.

This paper is organized as follows: we first derive the solidphase abundances of the primary elemental constituents of dust in Section 2; then, we combine various observational data to derive the wavelength dependence of dust extinction (Section 3), polarized extinction (Section 4), emission (Section 5), and polarized emission (Section 6) for a typical diffuse, high-latitude sight line. Finally, we present a summary of these constraints in Section 7.

### 2. Abundances

The heavy elements that make up the bulk of the mass of grains are produced in stars that return material to the ISM via winds or ejecta. Some of the atoms remain in the gas while a

fraction get locked in grains. Comparison of stellar and gasphase abundances of metals is thus an important observational constraint on grain models.

The elements C, O, Mg, Si, and Fe are depleted in the gas phase and compose most of the interstellar dust mass. In addition, Al, S, Ca, and Ni are also depleted and constitute a minor but nonnegligible fraction of the dust mass. A dust model should account for the observed depletions of each of these elements. Other elements (e.g., Ti) are also present in the grains, but collectively account for <1% of the grain mass and will not be discussed here.

While gas-phase abundances are determined directly from absorption-line spectroscopy, inferring the solid-phase abundances from these measurements requires determination of the total abundance of each element in the ISM. This is often done starting from the well-constrained solar abundances and applying a correction for Galactic chemical enrichment (GCE) during the  $\sim$ 4.6 Gyr since the formation of the Sun.

Detailed 3D hydrodynamical modeling of the solar atmosphere has yielded photospheric abundances of  $\log \epsilon_{\rm C}=8.43\pm0.05$ ,  $\log \epsilon_{\rm O}=8.69\pm0.05$ ,  $\log \epsilon_{\rm Mg}=7.59\pm0.04$ ,  $\log \epsilon_{\rm Al}=6.43\pm0.04$ ,  $\log \epsilon_{\rm Si}=7.51\pm0.03$ ,  $\log \epsilon_{\rm S}=7.12\pm0.03$ ,  $\log \epsilon_{\rm Ca}=6.32\pm0.03$ ,  $\log \epsilon_{\rm Fe}=7.47\pm0.04$ , and  $\log \epsilon_{\rm Ni}=6.20\pm0.04$  (Asplund et al. 2009; Scott et al. 2015a, 2015b), where

$$\log \epsilon_{\rm X} \equiv 12 + \log_{10}({\rm X/H}) \tag{1}$$

and (X/H) is the number of atoms of element X per H atom. To convert these present-day photospheric abundances to protosolar abundances, we apply a diffusion correction of +0.03 dex (Turcotte & Wimmer-Schweingruber 2002). We adopt these values as our reference protosolar abundances.

The protosolar values are presumed to reflect the abundances in the ISM at the time of the Sun's formation 4.6 Gyr ago. Present-day interstellar metal abundances are likely enhanced relative to these protosolar values. The chemical evolution model of Chiappini et al. (2003, Model 7) predicts the C, O, Mg, Si, S, and Fe abundances to be enriched by 0.06, 0.04, 0.04, 0.08, 0.09, and 0.14 dex, respectively, relative to the protosolar values. Bedell et al. (2018) estimated the chemical enrichment as a function of time by determining the elemental abundances in solar twins of various ages. If we assume  $\Delta$ [Fe/ H] = 0.14 (Chiappini et al. 2003), their results imply presentday enrichments of 0.05, 0.11, 0.10, 0.08, 0.11, 0.09, 0.16, and 0.09 dex for C, O, Mg, Al, Si, S, Ca, and Ni respectively, where in the case of C, we have taken the weighted mean of the determinations based on CI and CH. These results are summarized in Table 1. We apply the latter values to our reference protostellar abundances to define our reference ISM abundances, listed in the second column of Table 2.

Interstellar abundances can also be inferred from observations of young stars. Studies of young (<1 Gyr) F and G stars (Bensby et al. 2005; Bensby & Feltzing 2006) have yielded fairly concordant numbers for O, Mg, Al, Si, S, Ca, Fe, and Ni (see Lodders et al. 2009 for a review). The C abundance, however, appears somewhat lower than would be predicted from the solar abundances. On the other hand, Sofia & Meyer (2001) report C, O, Mg, Si, and Fe abundances obtained from young ( $\leq$ 2 Gyr) F and G stars that are in good agreement with the protosolar abundances plus enrichment, including the C abundance.

 Table 1

 Interstellar Abundances of Selected Elements

Element	A (ppm)	Method	Reference(s)
C	$324 \pm 38$	Solar + Solar Twins	2, 6, 11
	$331\pm38$	Solar + GCE Model	2, 3, 6
	$358\pm82$	Young F & G Stars	1
	$245\pm62$	Young F & G Stars	5, 7
	$190\pm77$	B Stars	1
	$214\pm20$	B Stars	8
O	$682 \pm 79$	Solar + Solar Twins	2, 6, 11
	$575\pm66$	Solar + GCE Model	2, 3, 6
	$445 \pm 156$	Young F & G Stars	1
	$589 \pm 176$	Young F & G Stars	4, 7
	$350 \pm 133$	B Stars	1
	$575 \pm 66$	B Stars	8
Mg	$52.9 \pm 4.9$	Solar + Solar Twins	2, 10, 11
	$45.7 \pm 4.2$	Solar + GCE Model	2, 3, 10
	$42.7 \pm 17.2$	Young F & G Stars	1
	$44 \pm 21$	Young F & G Stars	4, 7
	$23 \pm 7.0$	B Stars	1
	$36.3 \pm 4.2$	B Stars	8
Al	$3.5 \pm 0.3$	Solar + Solar Twins	2, 10, 11
	$3.5 \pm 1.8$	Young F & G Stars	4, 7
Si	$44.6 \pm 3.1$	Solar + Solar Twins	5, 8
	$41.7 \pm 2.9$	Solar + GCE Model	2, 3, 10
	$39.9 \pm 13.1$	Young F & G Stars	1
	$41 \pm 22$	Young F & G Stars	4, 7
	$18.8 \pm 8.9$	B Stars	1
	$31.6 \pm 3.6$	B Stars	8
S	$17.2 \pm 1.2$	Solar + Solar Twins	2, 10, 11
	$17.4 \pm 1.2$	Solar + GCE Model	2, 3, 9
	$19.5 \pm 4.5$	Young F & G Stars	4, 7
Ca	$3.2 \pm 0.2$	Solar + Solar Twins	2, 10, 11
	$3.0 \pm 2.7$	Young F & G Stars	4, 7
Fe	$43.7 \pm 4.0$	Solar + GCE Model	2, 3, 9
-	$27.9 \pm 7.7$	Young F & G Stars	1
	$40.7 \pm 23.5$	Young F & G Stars	4, 7
	$28.5 \pm 18.0$	B Stars	1
	$33.1 \pm 2.3$	B Stars	8
Ni	$2.1 \pm 0.2$	Solar + Solar Twins	2, 9, 11
	$1.8 \pm 0.3$	Young F & G Stars	4, 7

**Note.** Abundances of selected elements derived from solar abundances (Refs. 6, 9, 10) corrected for diffusion (Ref. 2) and chemical enrichment (Refs. 3 and 11), from young F and G stars (Refs. 4, 5, and 7), and from B stars (Refs. 1 and 8).

**References.** (1) Sofia & Meyer (2001), (2) Turcotte & Wimmer-Schweingruber (2002), (3) Chiappini et al. (2003), (4) Bensby et al. (2005), (5) Bensby & Feltzing (2006), (6) Asplund et al. (2009), (7) Lodders et al. (2009), (8) Nieva & Przybilla (2012), (9) Scott et al. (2015a), (10) Scott et al. (2015b), (11) Bedell et al. (2018).

Photospheric abundances have also been determined for B stars with mostly consistent results, as summarized in Table 1. However, the Si abundances determined from B stars are somewhat lower, with reported values of  $18.8 \pm 8.9$  ppm (Sofia & Meyer 2001) and  $31.6 \pm 2.6$  ppm (Nieva & Przybilla 2012). Likewise, the Fe abundances are lower than those based on solar abundances by  $\sim 10$  ppm.

Different determinations of the interstellar metal abundances are not yet fully concordant, and the uncertainties quoted by any study using a specific class of objects may underrepresent the underlying systematic uncertainties particular to that method. For the purposes of this work, we adopt abundances based on solar abundances plus enrichment as representative.

 Table 2

 Adopted Gas- and Solid-phase Abundances of Selected Elements

X	(X/H) <sub>ISM</sub> (ppm)	(X/H) <sub>gas</sub> (ppm)	(X/H) <sub>dust</sub> (ppm)
C	324	198	$126 \pm 56$
0	682	434	$249 \pm 94$
Mg	52.9	7.1	$45.8 \pm 4.9$
Al	3.5	0.1	$3.4 \pm 0.3$
Si	44.6	6.6	$38.0 \pm 3.1$
S	17.2	9.6	$7.6 \pm 2.0$
Ca	3.2	0.1	$3.2 \pm 0.2$
Fe	43.7	0.88	$42.8 \pm 4.0$
Ni	2.1	0.04	$2.0\pm0.2$

**Note.** ISM abundances based on solar abundances (Asplund et al. 2009; Scott et al. 2015a, 2015b) corrected for diffusion (Turcotte & Wimmer-Schweingruber 2002) and with GCE as determined from observations of young F and G stars (Bedell et al. 2018). Gas-phase abundances taken from Jenkins (2009) assuming moderate depletion (i.e.,  $F_* = 0.5$ ).

Once the baseline interstellar abundances have been determined, absorption-line spectroscopy can be employed to determine the quantity of each element missing from the gas phase due to incorporation into grains. Compiling data over a large number of sight lines and gas species, Jenkins (2009) defined a parameter  $F_*$  that quantifies the level of depletion of all metals along that sight line.  $F_* = 0.5$ , roughly the median depletion in the Jenkins (2009) sample, corresponded to sight lines with mean  $n_{\rm H} \simeq 0.3~{\rm cm}^{-3}$ , appropriate for diffuse H I. Therefore, we adopt the gas-phase abundances for  $F_* = 0.5$  as representative for the diffuse sight lines of interest in this work.

In Table 2, we list the gas-phase abundances of C, O, Mg, Si, S, Fe, and Ni corresponding to  $F_* = 0.5$  and the relations for each element derived by Jenkins (2009). For Al and Ca, we assume the level of depletion is the same as for Fe.

With the ISM and gas-phase abundances constrained, we take the difference to determine the solid-phase abundances, which we list in Table 2. We estimate the error bars by adding in quadrature those from Table 1 and the errors on the gas-phase abundances inferred from Jenkins (2009). Models of interstellar dust should account for the solid-phase abundances presented here to within the observational and modeling uncertainties.

The relative solid-phase abundances of the elements in Table 2 typically have a moderate dependence on the level of depletion (i.e.,  $F_*$ ). However, the number of depleted O atoms relative to depletion of atoms like Si, Mg, and Fe is a strong function of the parameter  $F_*$ , which seems to require major changes in the composition of the grain material formed as depletion proceeds. We therefore caution that the solid-phase O abundance reported in Table 2 for our idealized average diffuse sight line is especially uncertain. The O abundance poses a significant challenge for dust models. Models that assume solid-phase O to reside primarily in silicate material and metal oxides have difficulty accounting for the quantity of oxygen that is missing from the gas phase (Jenkins 2009; Whittet 2010; Poteet et al. 2015).

## 3. Extinction

### 3.1. Introduction

Interstellar dust attenuates light through both scattering and absorption. "Extinction" refers to the sum of these processes,

and the wavelength dependence of interstellar extinction forms a key constraint on the properties of interstellar grains. Because interstellar dust preferentially extinguishes shorter wavelengths in the optical, the effects of extinction are often referred to as "reddening."

Extinction is typically measured in one of two ways. In the "pair method," the spectrum of a reddened star is compared to an intrinsic spectrum derived from a set of standard unreddened stars (e.g., Trumpler 1930; Bless & Savage 1972). Alternatively, the stellar spectrum and the interstellar extinction can be modeled simultaneously with the aid of theoretical stellar spectra (e.g., Fitzpatrick & Massa 2005; Schultheis et al. 2014; Fitzpatrick et al. 2019).

However, neither method readily yields the total extinction  $A_{\lambda}$ , where

$$A_{\lambda} \equiv 2.5 \log_{10} \frac{F_{\lambda}^{\text{int}}}{F_{\lambda}^{\text{obs}}},\tag{2}$$

 $F_{\lambda}^{\rm int}=L_{\lambda}/4\pi D^2$  is the intrinsic (i.e., unreddened) flux, and  $F_{\lambda}^{\rm obs}$  is the observed flux. However, if the wavelength dependence of the luminosity  $L_{\lambda}$  is presumed to be known, the differential extinction between two wavelengths is independent of distance D. Most empirical extinction curves are thus expressed as the "selective" extinction relative to a reference bandpass or wavelength  $\lambda_0$  and written as

$$E(\lambda - \lambda_0) \equiv A_{\lambda} - A_{\lambda_0}. \tag{3}$$

To remove the dependence on the dust column, this is often then normalized to selective extinction between two reference bandpasses or wavelengths, classically the Johnson B and V bands, e.g.,  $E(\lambda - V)/E(B - V)$ . The quantity

$$R_V \equiv \frac{A_V}{E(B-V)} \tag{4}$$

is commonly used to parameterize the shape of the extinction curve.

As noted by many authors (e.g., Blanco 1957; Maíz Apellániz et al. 2014; Fitzpatrick et al. 2019), the use of bandpasses rather than monochromatic wavelengths to normalize extinction curves becomes problematic at high precision because the measured extinction in a finite bandpass depends not just on the interstellar extinction law but also on the intrinsic spectrum of the object. We therefore focus where possible in this work on the spectroscopic or spectrophotometric determinations of the interstellar extinction law.

Because we are principally interested in connecting observations to the properties of interstellar grains, we express our synthesized representative extinction law in terms of optical depth  $\tau_{\lambda}$  rather than  $A_{\lambda}$ , which are related by

$$\tau_{\lambda} \equiv \ln \left( \frac{F_{\lambda}^{\text{int}}}{F_{\lambda}^{\text{obs}}} \right) = \frac{A_{\lambda}}{2.5 \log_{10} e} = \frac{A_{\lambda}}{1.0857}.$$
 (5)

### 3.2. X-Ray Extinction

Although measurement of absolute extinction is usually not possible at X-ray energies, the differential extinction associated with X-ray absorption features can be determined spectroscopically. Such spectroscopic measurements have been made across the O K edge at  $530 \, \text{eV}$  (e.g., Takei et al. 2002), Fe L edge at  $\sim 700-750 \, \text{eV}$  (e.g., Paerels et al. 2001; Lee et al. 2009),

Mg K edge at 1.3 keV (e.g., Rogantini et al. 2020), and Si K edge at 1.84 keV (Schulz et al. 2016; Zeegers et al. 2017; Rogantini et al. 2020). Chandra and XMM-Newton both have sufficient spectral resolution to distinguish gas-phase absorption from extinction contributed by dust.

X-ray spectra have been interpreted as showing that interstellar silicates are Mg rich (Costantini et al. 2012; Rogantini et al. 2019), and Westphal et al. (2019) conclude that most of the Fe is in metallic form. While the absorption profile of the  $10 \mu m$  silicate feature has been interpreted as giving a 2% upper limit on the crystalline fraction (see Section 3.7), X-ray observations of the Mg and Si K edges have been interpreted as showing that 11%–15% of the silicate material is crystalline (Rogantini et al. 2019, 2020).

Efforts to identify the specific minerals hosting the solid-phase C, O, Mg, Si, and Fe remain inconclusive because of not-quite-sufficient spectral resolution, limited signal-to-noise ratio, and limited laboratory data. Scattering contributes significantly to the extinction (Draine 2003b), and therefore model comparisons depend not only on the composition of the dust, but also on the size and shape of the grains (Hoffman & Draine 2016). Future measurements of X-ray extinction and X-ray scattering (see Section 3.11.1) offer the prospect of mineralogical identification. The key will be to interpret the observations using dust models together with all available observational constraints.

### 3.3. UV Extinction

Spectroscopy from the International Ultraviolet Explorer (IUE) has been one of the primary data sets for characterizing the interstellar extinction law in the UV since the 1980s (e.g., Witt et al. 1984a; Fitzpatrick & Massa 1986, 1988; Cardelli et al. 1989; Valencic et al. 2004). Other notable measurements of UV extinction have been made by the Copernicus satellite (e.g., Cardelli et al. 1989), the Orbiting and Retrievable Far and Extreme Ultraviolet Spectrometer (ORFEUS; Sasseen et al. 2002), the Hubble Space Telescope (HST; e.g., Clayton et al. 2003), and the Far Ultraviolet Spectroscopic Explorer (FUSE; e.g., Gordon et al. 2009). Extinction in the UV is characterized by a steep rise to short wavelengths, a prominent broad spectral feature at 2175 Å (see Section 3.8.1), and a notable lack of other substructure (Clayton et al. 2003; Gordon et al. 2009).

Spectroscopic characterization of interstellar extinction from UV to optical wavelengths was recently undertaken by Fitzpatrick et al. (2019), who used HST Space Telescope Imaging Spectrograph (STIS) spectroscopy extending from 290–1027 nm to complement IUE UV data. Additionally, *JHK* photometry from the Two-Micron All Sky Survey (2MASS) was used to extend the analysis into the NIR. On the basis of these data toward a curated sample of 72 O and B stars, they derived a mean extinction law having A(5500 Å)/E(4400 Å-5500 Å)=3.02, corresponding approximately to  $R_V=3.1$ . Because of the narrowband observations, the resulting extinction curve is monochromatic and normalized using the extinction at 4400 and 5500 Å rather than the Johnson B and V bands, respectively. We illustrate this curve in Figures 1 and 2.

On the basis of UV, optical, and NIR data toward a sample of 45 stars studied in the UV by Fitzpatrick & Massa (1988), Cardelli et al. (1988) presented an analytic parameterization for the extinction for  $\lambda^{-1}$  between 3.3 and 8  $\mu$ m<sup>-1</sup> as a function of  $R_V$ . This law was extended to the range 0.3–10  $\mu$ m<sup>-1</sup> by Cardelli et al. (1989). Combining IUE spectroscopy and 2MASS data

along 417 lines of sight, Valencic et al. (2004) further refined this parameterization in the  $3.3{\text -}8.0\,\mu\text{m}^{-1}$  range.<sup>2</sup> We note, however, that the extinction law in this range was not formulated to join smoothly with the adjacent sections of the extinction law parameterized by Cardelli et al. (1989). Finally, Gordon et al. (2009) used the functional form<sup>3</sup> presented in Cardelli et al. (1989) to fit 75 extinction curves measured with FUSE data from 3.3 to  $11\,\mu\text{m}^{-1}$ .

We include the extinction laws of Cardelli et al. (1989), Valencic et al. (2004), and Gordon et al. (2009) in Figure 1. These extinction laws were derived in terms of  $E(\lambda - V)/E(B - V)$  rather than monochromatic equivalents. Applying the correction factors to account for the finite bandpasses suggested by Fitzpatrick et al. (2019; Equation (4)) results in curves that deviate more substantially from unity at 4400 Å and zero at 5500 Å than applying no correction. It is also the case that the  $R_V = 3.1$  curve using the Cardelli et al. (1989) parameterization does not precisely have  $A_V/E(B - V) = 3.1$  (see discussion in Maíz Apellániz 2013). Given these issues, we simply assume that E(B - V) corresponds exactly to E(4400 Å-5500 Å) to convert the  $R_V = 3.1$  curves to monochromatic reddenings.

Sasseen et al. (2002) made a determination of the mean FUV (910–1200 Å) extinction law using observations of 11 pairs of B stars with the ORFEUS spectrometer. This curve is also plotted in Figure 1 where, as with several of the other curves presented, we do not apply any corrections to translate from the reported  $E(\lambda - V)/E(B - V)$  to monochromatic reddenings. While the shape of this curve is in general agreement with that of Cardelli et al. (1989) and Gordon et al. (2009), there is significantly less FUV extinction per E(B - V).

As Figure 1 illustrates, there is general agreement among extinction curves in the UV. The Fitzpatrick et al. (2019) and Gordon et al. (2009) curves correspond closely between 3.3 and 6  $\mu$ m<sup>-1</sup>, while that of Valencic et al. (2004) agrees better with that of Fitzpatrick et al. (2019) between 5 and 8  $\mu$ m<sup>-1</sup>. For our representative extinction curve, we therefore employ the Fitzpatrick et al. (2019) curve from 5500 Å to 8  $\mu$ m<sup>-1</sup>, and then match onto the curve of Gordon et al. (2009) to extend to 11  $\mu$ m<sup>-1</sup>. This is accomplished by using the Cardelli et al. (1989) curve between 8 and 10  $\mu$ m<sup>-1</sup>.

# 3.4. Optical Extinction

While the extinction curve of the diffuse ISM has been well determined from UV to optical wavelengths over decades of observations, it is only recently that spectrophotometric observations have enabled detailed characterization at optical wavelengths. In this section, we compare determinations of the mean Galactic extinction curve from 500 nm to 1  $\mu$ m.

In addition to Fitzpatrick et al. (2019), a recent determination of the optical extinction law using spectroscopy is that of Maíz Apellániz et al. (2014), who used the Fibre Large Array Multi-Element Spectrograph (FLAMES) on the Very Large Telescope to determine the extinction toward 83 O and B stars in 30 Doradus. These spectroscopic data extended from 3960 to 5071 Å and were supplemented with both 2MASS JHK and HST Wide Field Camera 3 photometry (UBVI and  $H\alpha$ ) to test and revise the Cardelli et al. (1989) extinction law from the optical to the NIR. Outside this wavelength range, Maíz Apellániz et al. (2014) tied the extinction law to that of Cardelli et al. (1989). The

Note corrected numbers in Valencic et al. (2014).

Note corrected numbers in Gordon et al. (2014).

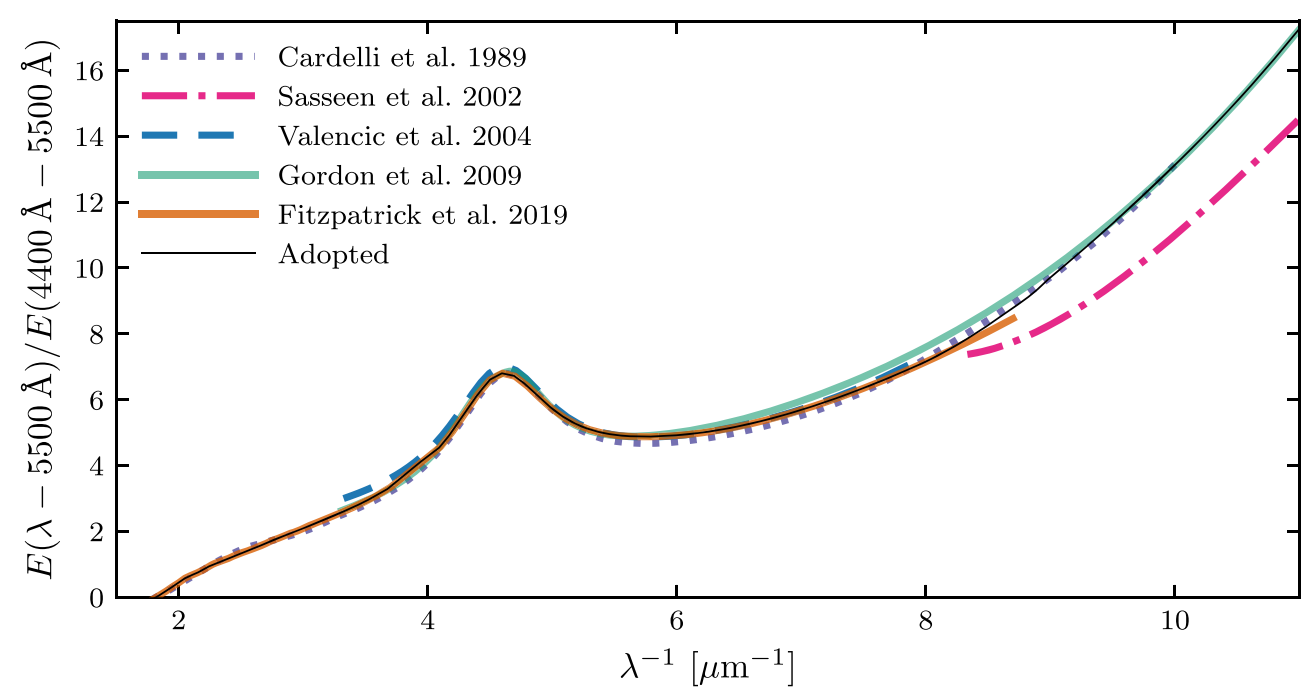
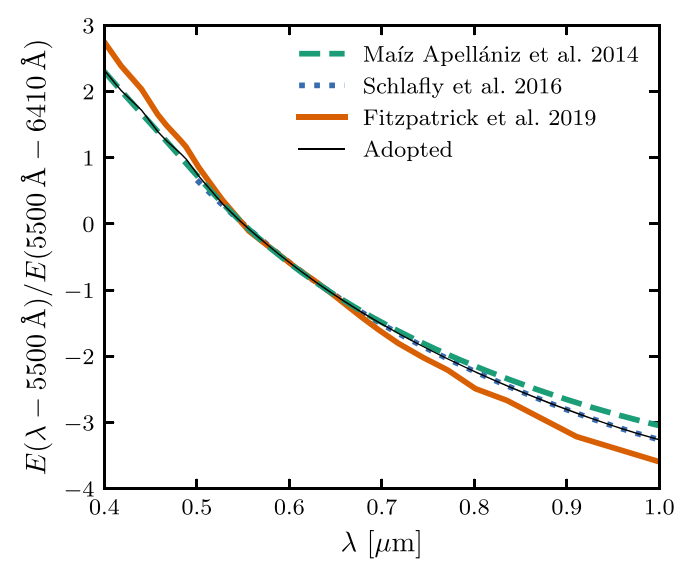


Figure 1. We present various determinations of the UV extinction curve of the diffuse Galactic ISM. The extinction law of Fitzpatrick et al. (2019; orange solid) was derived in terms of monochromatic reddenings. However, those of Cardelli et al. (1989; purple dotted), Sasseen et al. (2002; magenta dotted–dashed), Valencic et al. (2004; blue dashed), and Gordon et al. (2009; green solid) were derived with respect to finite bandpasses, i.e.,  $E(\lambda - V)/E(B - V)$ . As discussed in the text, we present these curves by simply assuming perfect correspondence with  $E(\lambda - 5500 \text{ Å})/E(5500 \text{ Å}-6410 \text{ Å})$ .



**Figure 2.** The extinction laws of Maíz Apellániz et al. (2014; green dashed), Schlafly et al. (2016; blue dotted), and Fitzpatrick et al. (2019; orange solid) are compared at optical wavelengths. The normalization corresponds roughly to E(V-R), which we adopt because the Schlafly et al. (2016) curve does not extend to wavelengths shorter than 500 nm.

resulting curve is presented in Figure 2 alongside that of Fitzpatrick et al. (2019). While there is general consistency between the two extinction laws, there are also significant departures. As 30 Doradus is located in the Large Magellanic Cloud (LMC), the extinction has a contribution from the LMC dust, which may differ systematically from that of the Galaxy. We therefore seek comparisons with other observations.

Schlafly et al. (2016) determined the extinction toward 37,000 APOGEE stars in 10 photometric bands from g (503.2 nm) to WISE 2 (4.48  $\mu$ m). This wavelength coverage

does not extend far enough blueward to apply the normalization used in Figure 1, and indeed Schlafly et al. (2016) note that different methods of extrapolating their extinction law to the B band yield  $R_V$  that differ by a few tenths. Thus, Figure 2 presents a different comparison using E(5500 Å-6410 Å) as the normalization factor, roughly equivalent to E(V-R). Because of the explicit treatment of the bandpasses, the Schlafly et al. (2016) extinction curve is defined with respect to monochromatic wavelengths.

From 500 to  $\sim$ 800 nm, the Maíz Apellániz et al. (2014) and Schlafly et al. (2016) curves are in close agreement. We note that the Maíz Apellániz et al. (2014) extinction law defaults to that of Cardelli et al. (1989) at wavelengths longer than  $\sim$ 800 nm. Indeed, Schlafly et al. (2016) note that the Cardelli et al. (1989) parameterization provides a poor fit to the infrared data for the full range of  $R_V$  studied while the Maíz Apellániz et al. (2014) law is an excellent fit in the optical.

Wang & Chen (2019) employed Gaia parallaxes for a sample of more than 61,000 red clump stars in APOGEE to overcome the distance/attenuation degeneracy and derive a mean interstellar extinction law in 21 photometric bands. When expressed as color excess ratios  $E(\lambda - \lambda_{\rm l})/E(\lambda_{\rm 2} - \lambda_{\rm l})$ , their mean curve agrees with that of Schlafly et al. (2016) to within a few percent over the full 0.5–4.5  $\mu$ m wavelength range.

Given these corroborating studies, we adopt the extinction law of Schlafly et al. (2016) from 550 nm to the IR. However, converting from  $E(\lambda - 5500 \text{ Å})/E(4400 \text{ Å}-5500 \text{ Å})$  to a quantity like  $A_{\lambda}/A(5500 \text{ Å})$  requires a measurement of the absolute extinction at some wavelength. This is because a single reddening law is consistent with a family of extinction laws that differ by an additive offset common to all wavelengths over which the reddening has been measured. The classic  $R_V = 3.1$  is relatively well determined from the fact that the infrared extinction is much smaller than the optical and UV extinction,

and so measurement of reddening relative to an NIR band, e.g., E(V-L)/E(B-V), constrains any component common to all bands sufficiently well, i.e.,  $E(V-L)/E(B-V) \approx R_V$ . As determinations of the extinction curve are made at increasingly long wavelengths, the sensitivity to the size of this common component increases. We explore this issue in more detail in the following section.

### 3.5. NIR Extinction

The NIR extinction law from  $\sim 1-5 \, \mu \mathrm{m}$  is often approximated as a power law  $A_{\lambda} \propto \lambda^{-\alpha}$ . A foundational analysis of NIR extinction was made by Rieke & Lebofsky (1985), who measured extinction toward o Sco ( $A_V = 2.7$ , Whittet 1988), Cyg OB2-12 ( $A_V \simeq 10.2$ , Humphreys 1978; Torres-Dodgen et al. 1991), and several heavily reddened sources toward the Galactic Center ( $A_V$  between 23 and 35). The widely used extinction law of Cardelli et al. (1989) relies on the extinction curve determined by Rieke & Lebofsky (1985) at wavelengths longer than the J band ( $\lambda_J \simeq 1.23 \, \mu \mathrm{m}$ ), employing  $\alpha = 1.61$  for  $0.91 < \lambda/\mu \mathrm{m} < 3.3$ .

Many other early determinations of  $\alpha$  likewise found values in the range  $\sim$ 1.6–1.85 (see the reviews of Draine 1989b and Mathis 1990). However, an analysis by Stead & Hoare (2009) demonstrated that the value of  $\alpha$  derived from fits to extinction in the *JHK* photometric bands depends sensitively on how the bandpasses are treated, particularly for highly reddened sources. Accounting explicitly for these bandpass effects in sources of different intrinsic spectra and levels of reddening, and using photometry from both the United Kingdom Infrared Deep Sky Survey (UKIDSS) and 2MASS, they recommend a mean value of  $\alpha = 2.15 \pm 0.05$ , significantly larger than most earlier determinations. Recently, a similar study using 2MASS photometry found  $\alpha = 2.27$  with an uncertainty of  $\sim$ 1% (Maíz Apellániz et al. 2020).

While the power-law approximation is both simple and effective, Fitzpatrick & Massa (2009) demonstrated that extinction between the I ( $\lambda_I \simeq 0.798~\mu m$ ) and  $K_s$  ( $\lambda_{K_s} \simeq 2.16~\mu m$ ) bands is better represented by a modified power law in which  $\alpha$  increases between 0.75 and 2.2  $\mu m$ . They proposed instead a function of the form

$$\frac{A_{\lambda}}{E(B-V)} \propto \frac{1}{1 + (\lambda/\lambda_0)^{\gamma}},$$
 (6)

with  $\lambda_0=0.507~\mu m$ . The fit values of  $\gamma$  varied considerably from sight line to sight line, ranging from  $\sim 1.8$  to 2.8, and the constant of proportionality was found to depend on  $R_V$ . Schlafly et al. (2016) found excellent agreement in the NIR between this parameterization with  $\gamma\simeq 2.5$  and their mean extinction law. While this functional form captures the flattening of the extinction law at the shortest wavelengths in this range, other studies have noted an apparent flattening of the NIR extinction law at the longest wavelengths as well, particularly in comparing the slope of the extinction curve between J and H ( $\lambda_H \simeq 1.63~\mu m$ ) to the slope between H and  $K_s$  (e.g., Fritz et al. 2011; Hosek et al. 2018; Nogueras-Lara et al. 2020). Such behavior is not unexpected given indications of a relatively flat MIR extinction curve (see Section 3.6).

The assumption of a power law can have a dramatic effect on the conversion from reddening to extinction. If  $A_{\lambda} \propto \lambda^{-\alpha}$ , then

$$\frac{E(J-H)}{E(H-K)} = \frac{\left(\frac{\lambda_H}{\lambda_J}\right)^{\alpha} - 1}{1 - \left(\frac{\lambda_H}{\lambda_K}\right)^{\alpha}}.$$
 (7)

With a sample of 37,000 stars, Schlafly et al. (2016) made precise determinations of interstellar reddening in these bands. Inserting their measured reddenings into Equation (7) yields  $\alpha = 2.30$ . As discussed in Section 3.4, however, a single reddening law is consistent with a family of extinction laws that differ by an additive constant. One method of placing a limit on this constant is to require the extinction in the longest wavelength band to be positive. Another more constraining method is to find the additive constant such that the ratio of the extinction in two bands agrees with a measured value. We find that  $\alpha \simeq 2.30$  between J and K can be achieved by employing the Schlafly et al. (2016) reddening law and imposing  $A_H/A_K = 1.87$ . However, this same reddening law is consistent with a (wavelength-dependent) logarithmic slope of  $\sim$ 1.7 in the NIR when instead requiring  $A_H/A_K=1.55$  (as determined by Indebetouw et al. 2005).

It is therefore unclear whether the large values of  $\alpha$  found by Stead & Hoare (2009) and Maíz Apellániz et al. (2020) are indeed more physical due to the more careful treatment of the bandpasses or whether they are biased toward higher values of  $\alpha$  by forcing extinction in the *JHK* bands to conform precisely to a power law. An independent constraint on the absolute extinction is needed to break this degeneracy.

The default curve put forward by Schlafly et al. (2016) employs  $A_H/A_K = 1.55$  as determined by Indebetouw et al. (2005). In that study, the absolute extinction was constrained along diffuse sight lines in the Galactic plane with  $\ell \simeq 42^{\circ}$  by measuring the extinction toward K giants, which are well localized in color space, under the assumption that extinction per unit distance is constant in the Galactic plane. Wang & Chen (2019) used Gaia parallaxes to measure the reddening as a function of distance modulus toward a sample of more than 60,000 red clump stars. They found  $A_H/A_{K_s}=1.75$ , noting agreement with Chen et al. (2018), who used 55 classical Cepheids to measure distance to the Galactic Center and derived  $A_H/A_{K_s} = 1.717$ . Photometry of red clump stars toward the Galactic Center has yielded relatively concordant values of  $\sim$ 1.69  $\pm$  0.03 (Nishiyama et al. 2006; Nagatomo et al. 2019),  $1.76\pm0.10$  (Schödel et al. 2010), and  $1.84\pm0.03$  (Nogueras-Lara et al. 2020).

The steep NIR extinction laws implied by large values of  $A_H/A_K$  are difficult to reconcile with relatively flat extinction between 4 and 8  $\mu$ m and comparisons between visual extinction and extinction in the 9.7  $\mu$ m feature, as we discuss in the next section. The NIR extinction is sensitive to the relative abundance of the largest interstellar grains, and so sight lines passing through molecular gas, where grains grow to larger sizes through coagulation, may have systematically different properties. It is unclear if this effect is responsible for the discrepancy between the observations of Indebetouw et al. (2005) on a relatively diffuse sight line and those toward the Galactic Center.

Ultimately, on the basis of the observed properties of the MIR extinction, we adopt as our representative NIR extinction

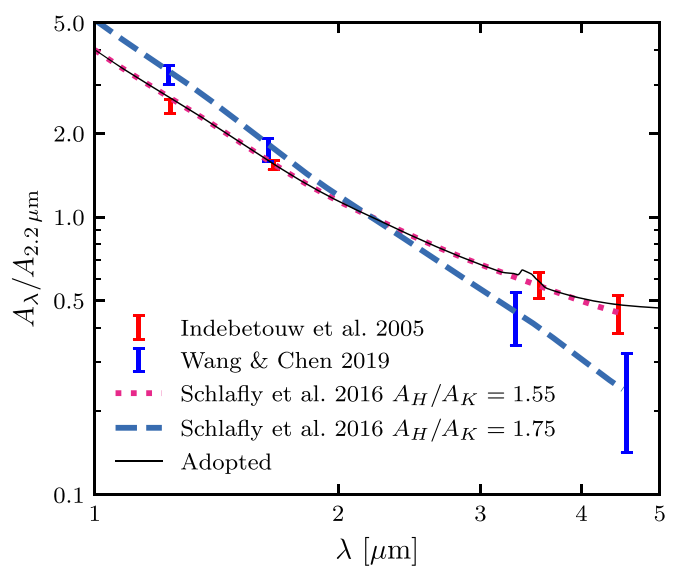


**Figure 3.** We compare the NIR/MIR broadband extinction curves of Indebetouw et al. (2005) along a diffuse sight line in the Galactic plane ( $\ell=42^{\circ}$ ) and Wang & Chen (2019) toward a sample of more than 61,000 red clump stars in the APOGEE survey. For both of these curves, we report extinction relative to the  $K_s$  band. We compare these determinations to the Schlafly et al. (2016) reddening law assuming two values of  $A_H/A_K$ : 1.55 from Indebetouw et al. (2005) and 1.75, a representative average of recent measurements (see Section 3.5).

curve the reddening law of Schlafly et al. (2016) with  $A_H/A_K = 1.55$  to convert to extinction. We present the resulting extinction law in Figure 3, where we compare it to the same reddening law derived assuming  $A_H/A_K = 1.75$  instead. Further studies of NIR extinction along diffuse sight lines are needed to clarify the steepness of the interstellar extinction curve and its variations with the local environment.

### 3.6. MIR Extinction

The MIR extinction is dominated by continuum extinction between 3 and 8  $\mu$ m and by the 9.7 and 18  $\mu$ m silicate features longward of 8  $\mu$ m. We focus here on the former, deferring discussion of the silicate features to Section 3.7. Carbonaceous MIR extinction features are discussed in Section 3.8.2.

Some early determinations of the MIR extinction suggested a continuation of the NIR power law with a sharp minimum at 7  $\mu$ m (e.g., Rieke & Lebofsky 1985; Bertoldi et al. 1999; Rosenthal et al. 2000; Hennebelle et al. 2001). However, a growing body of work suggests that the MIR extinction is relatively flat between  $\sim$ 4 and 8  $\mu$ m across a diversity of sight lines and values of  $R_V$ .

Sight lines toward the Galactic Center have been well measured in extinction and were the first to suggest, via observation of hydrogen recombination lines, a flattening of the extinction law in the MIR (Lutz et al. 1996; Lutz 1999). Subsequent broadband and spectroscopic observations toward the Galactic center (Nishiyama et al. 2006, 2008, 2009; Fritz et al. 2011) and the Galactic plane (Jiang et al. 2003, 2006; Gao et al. 2009) have proven to be consistent with a relatively flat extinction law. Likewise, Flaherty et al. (2007) found good agreement with the Lutz et al. (1996) extinction curve when measuring the extinction toward nearby star-forming regions where the extinction was dominated by molecular gas. Observing in the dark cloud Barnard 59 ( $A_K \sim 7$ ,  $A_V \sim 59$ ),

Román-Zúñiga et al. (2007) measured a  $1.25-7.76 \mu m$  extinction law consistent with that of Lutz et al. (1996).

We seek the properties of dust in the diffuse ISM, which may be systematically different from these more heavily extinguished sight lines. However, the relatively flat extinction law between  $\sim 3$  and 8  $\mu m$  appears fairly universal. Combining Spitzer and 2MASS observations on an "unremarkable" region in the Galactic plane centered on  $\ell = 42^{\circ}$ ,  $b = 0.5^{\circ}$ , Indebetouw et al. (2005) derived a extinction curve in agreement with Lutz et al. (1996). Zasowski et al. (2009) derived an average extinction curve over 150° in the Galactic midplane also using Spitzer and 2MASS photometry, finding excellent agreement with Indebetouw et al. (2005). Further, they note consistency between their result and extinction curves in low-extinction regions in molecular clouds measured by Chapman et al. (2009). Wang et al. (2013) measured the IR extinction law in regions of the Coalsack nebula that sampled a range of environments from diffuse to dark, finding a relatively universal shape of the MIR extinction across environments. Xue et al. (2016) derived a relatively flat MIR extinction curve toward a sample of G and K giants in the Spitzer IRAC bands, in agreement with recent studies and sharply discrepant with a deep minimum in the extinction curve at  $\sim$ 7  $\mu$ m.

The Spitzer Infrared Spectrograph (IRS) enables spectroscopic determination of the extinction law from  $\sim$ 5 to 37  $\mu$ m. Employing IRS spectra toward a sample of five O and B stars, Shao et al. (2018) derived a relatively flat extinction curve between 5 and 7.5  $\mu$ m. Also using IRS data, Hensley & Draine (2020) determined a nearly identical extinction curve toward Cyg OB-12 in the 5–8  $\mu$ m range.

On the basis of these data, we conclude that a relatively flat extinction curve between  $\sim 4$  and 8  $\mu m$  is universal and typical of even the diffuse ISM having  $R_V \approx 3.1$ , not just sight lines with large values of  $R_V$ . We summarize a selection of these observations in Figure 4. It must be cautioned, however, that the conversion from reddenings to extinction in many of these studies was accomplished by assuming a power-law form in the NIR, and thus uncertainty still remains in both the precise shape and amount of 4–8  $\mu m$  extinction relative to the NIR.

To create a composite extinction law, we join the Schlafly et al. (2016) curve (with  $A_H/A_K=1.55$ ) described in Section 3.5 to the extinction measured toward Cyg OB2-12 by Hensley & Draine (2020). The latter study presented a synthesized extinction curve by joining the measured 6–37  $\mu$ m extinction inferred from Spitzer IRS measurements to the Schlafly et al. (2016) extinction law likewise assuming  $A_H/A_K=1.55$ . As illustrated in Figure 4, this provides a good representation of other studies of extinction in the 4–8  $\mu$ m range.

As discussed in Section 3.5,  $A_H/A_K = 1.55$  is low relative to several recent determinations, which favor a value of  $\simeq 1.75$ . On the other hand, the Schlafly et al. (2016) extinction law having  $A_H/A_K = 1.75$  shows no evidence for flattening even out to 4.5  $\mu$ m and implies lower 4–8  $\mu$ m extinction relative to K band than inferred from a number of studies (see Figure 4). As we discuss in the following section, our adopted extinction curve has a value of  $A_V/\Delta \tau_{9.7} = 20.0$ , at the upper end of the observed range ( $\sim 18.5 \pm 2$ , Draine 2003a). Joining a representative MIR extinction profile to an NIR extinction law with a higher value of  $A_H/A_K$  would result in a larger  $A_V/\Delta \tau_{9.7}$ , exacerbating this tension. More work is needed to fully reconcile the existing observations of NIR and MIR

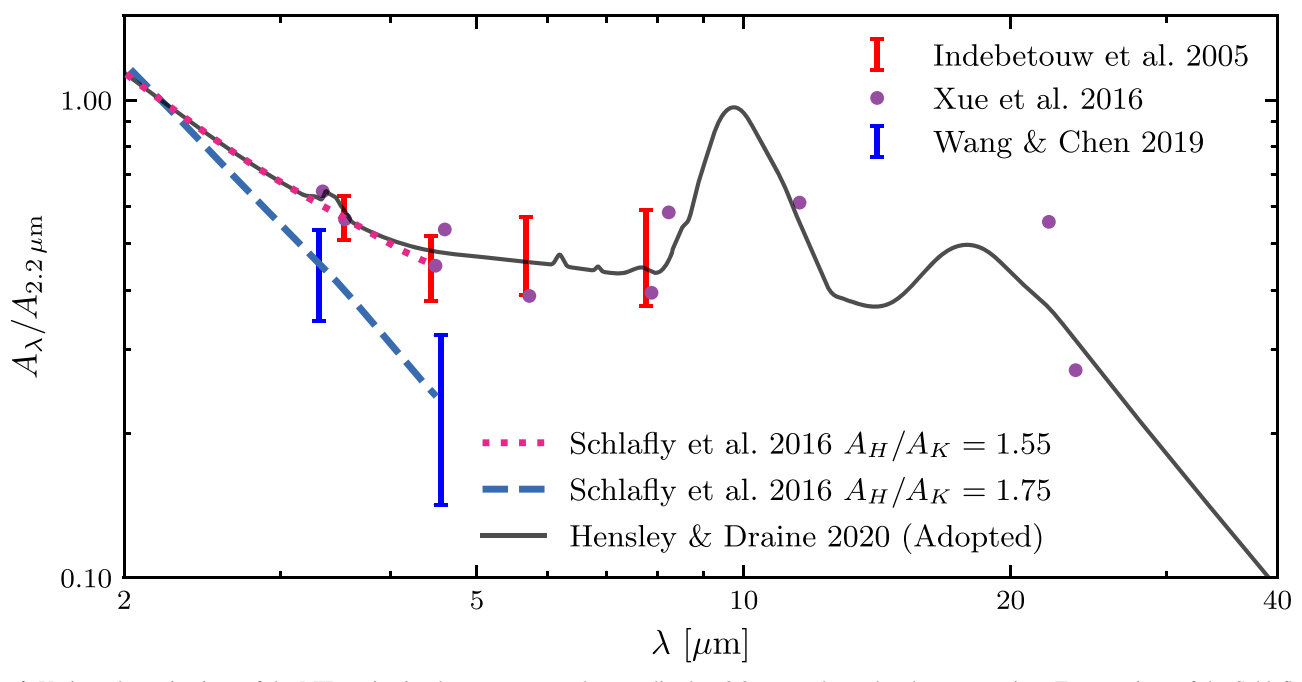


Figure 4. Various determinations of the MIR extinction law are presented, normalized to  $2.2~\mu m$  or the  $K_s$  band as appropriate. Two versions of the Schlafly et al. (2016) curve are shown, one assuming  $A_H/A_K=1.55$  (dotted) and the other 1.75 (dashed). The extinction toward Cyg OB2-12 based on ISO-SWS and Spitzer IRS data is shown in black (Hensley & Draine 2020) and is the basis of our synthesized extinction curve for  $\lambda>2.2~\mu m$ . Note that it matches onto the Schlafly et al. (2016) curve with  $A_H/A_K=1.55$  by design. We also present a few representative broadband determinations using combinations of Spitzer IRAC, WISE, and AKARI photometry, including Indebetouw et al. (2005; red error bars), Xue et al. (2016;  $A_{K_s}<0.5$  sample, purple circles), and Wang & Chen (2019; blue error bars).

extinction, and we thus present our synthesized curve as only our current best estimate of the true interstellar extinction.

Finally, we note that Schlafly et al. (2016) determined the interstellar extinction only in broad photometric bands and thus their resulting extinction curve does not contain spectral features. In contrast, Hensley & Draine (2020) used spectroscopic ISO-SWS data to determine the profile of the the 3.4  $\mu$ m spectroscopic feature toward Cyg OB2-12, which can be seen in Figure 4. We discuss this and other other spectroscopic features in greater detail in the following sections.

### 3.7. Silicate Features

In addition to the smooth continuum extinction provided by the ensemble of interstellar dust grains, there are well-studied extinction features attributable to specific grain species. Prominent among these are features at 9.7 and 18  $\mu$ m that have been identified with silicate material, the former arising from the Si–O stretching mode and the latter from the O–Si–O bending mode.

The 9.7  $\mu$ m feature was discovered as a circumstellar emission feature (Gillett et al. 1968; Woolf & Ney 1969). Woolf & Ney (1969) demonstrated that the feature was consistent with the expected behavior of silicate material, a claim strengthened by the discovery of a second feature at 18  $\mu$ m (Forrest et al. 1979). Subsequent observations have revealed that these features are not only found in circumstellar emission but are also ubiquitous in absorption in the diffuse ISM (see, e.g., van Breemen et al. 2011).

The sight line to the Galactic Center has enabled the detailed study of both the 9.7  $\mu$ m (Roche & Aitken 1985; Smith et al. 1990; Kemper et al. 2004) and 18  $\mu$ m features (McCarthy et al. 1980) by virtue of its substantial dust column. Roche & Aitken (1985) found that the *V*-band extinction relative to the optical depth  $\Delta \tau_{9.7}$  of the silicate feature at 9.7  $\mu$ m has a value of

 $A_V/\Delta au_{9.7}=9\pm1$ . Kemper et al. (2004) employed ISO observations toward two carbon-rich Wolf–Rayet stars located toward the Galactic Center to derive the profile of the 9.7  $\mu$ m silicate feature  $\Delta au_{\lambda}/\Delta au_{9.7~\mu m}$ , which we plot in Figure 5.

With heavy visual extinction ( $A_V \simeq 10.2$  mag; Humphreys 1978; Torres-Dodgen et al. 1991) and yet a lack of ice features, the sight line toward the blue hypergiant Cyg OB2-12 is ideal for studying extinction arising from the diffuse atomic ISM (Whittet 2015). The 9.7  $\mu$ m silicate feature on this sight line was first observed by Rieke (1974), and subsequent observations have produced detailed determinations of the both the 9.7 and 18  $\mu$ m silicate features (Whittet et al. 1997; Fogerty et al. 2016; Hensley & Draine 2020). In Figure 5, we compare the Cyg OB2-12 feature profile determined by Hensley & Draine (2020) to that of the Galactic Center (Kemper et al. 2004) and a sample of O and B stars (Shao et al. 2018).

The agreement between these profiles corroborates other studies noting a relatively universal silicate feature profile in the diffuse ISM (e.g., Chiar & Tielens 2006; van Breemen et al. 2011). Interstellar dust models should therefore be compatible with this profile, which has FWHM  $\simeq$ 2.2  $\mu$ m. As noted by Chiar & Tielens (2006), this average feature profile is narrower than the profile seen in emission toward the Trapezium region (FWHM  $\simeq$ 3.45  $\mu$ m, Forrest et al. 1975), which was used to calibrate some models (e.g., Draine & Lee 1984).

Dust models should also be able to reproduce the observed strength of the feature. The extinction curve we synthesize in this work has  $A_{5500~\text{Å}}/\Delta\tau_{9.7}=20.0$ . Comparing a variety of measurements toward Wolf–Rayet stars and toward Cyg OB2-12, Draine (2003a) suggested a mean value  $A_V/\Delta\tau_{9.7}=18.5\pm2$ , consistent with our composite curve.

Determination of the  $18 \mu m$  feature profile is made difficult by uncertainty in the underlying continuum extinction (see discussion in van Breemen et al. 2011; Hensley & Draine 2020).

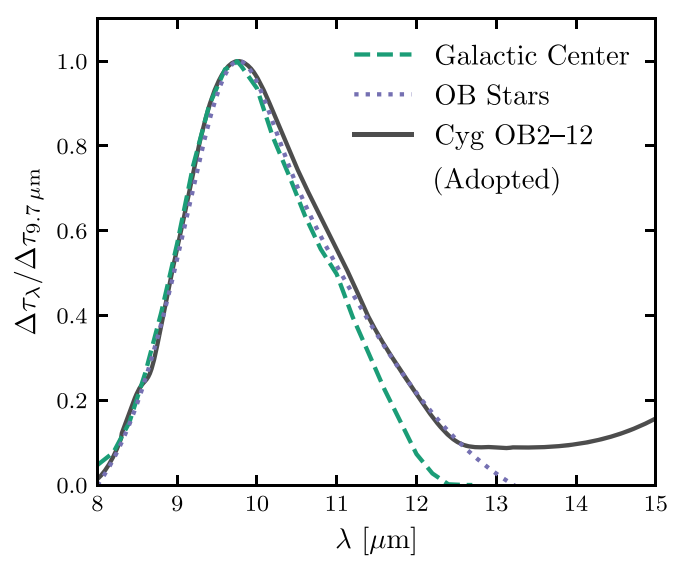


**Figure 5.** We compare three determinations of the profile of the 9.7  $\mu$ m silicate feature on different sight lines: toward the Galactic Center (Kemper et al. 2004), a sample of five O and B stars (Shao et al. 2018), and Cyg OB2-12 (Hensley & Draine 2020). The agreement between these profiles suggests a universality of the silicate feature throughout the ISM. Residual differences between the profiles may be attributable to different treatments of the underlying continuum extinction.

 $\Delta au_{18}/\Delta au_{9.7}$  is typically found to be of order 0.5 (Chiar & Tielens 2006; van Breemen et al. 2011; Hensley & Draine 2020). In performing model fits to the emission from Cyg OB2-12 and its stellar wind, Hensley & Draine (2020) required that the extinction longward of 18  $\mu$ m extrapolate to values estimated from the FIR emission. Further, this extrapolation was required to have a functional form consistent with power-law fits to the FIR emission. Thus, while the 18  $\mu$ m feature itself is difficult to isolate from the total extinction, the long-wavelength behavior of the extinction curve synthesized here is both physically and empirically motivated and serves as a reasonable best estimate.

Just as the presence of the 9.7 and  $18\,\mu\mathrm{m}$  silicate features constrains grain models, the absence of certain features likewise informs our understanding of the composition of interstellar dust. The  $11.2\,\mu\mathrm{m}$  feature arising from silicon carbide (SiC) is not observed to low detection limits, which appears to constrain the amount of Si in SiC dust to less that about 5% (Whittet et al. 1990). However, the SiC absorption profile is highly shape dependent, and irregularly shaped SiC grains could be abundant despite the nondetection at  $11.2\,\mu\mathrm{m}$ . If the observed "shoulder" of the 9.7  $\mu\mathrm{m}$  feature is attributed to irregular SiC grains, as much as 9%–12% of the interstellar Si could be in the form of SiC (Whittet et al. 1990).

Little substructure has been detected in the 9.7  $\mu$ m silicate feature, indicating that the feature arises predominantly from amorphous rather than crystalline silicates. Toward Cyg OB2-12, Bowey et al. (1998) found minimal evidence for fine structure between 8.2 and 11.7  $\mu$ m except a possible weak feature at 10.4  $\mu$ m that may be attributable to crystalline serpentine. Measuring silicate absorption toward two protostars and finding a lack of fine structure, Demyk et al. (1999) determined that at most 1%–2% of the mass of the silicates giving rise to the feature in star-forming clouds could be crystalline, whereas Kemper et al. (2005) estimated that at most 2.2% of the silicate mass in the diffuse ISM could be crystalline. On the basis of detections of the 11.1  $\mu$ m feature from crystalline

forsterite in many interstellar environments, Do-Duy et al. (2020) concluded that  $\sim 1.5\%$  of the silicate mass in the diffuse ISM is crystalline, which is consistent with previously derived upper limits. To the extent that the weak, broad 11.1  $\mu$ m feature is present in the extinction toward Cyg OB2-12, it is implicitly included in the representative extinction curve we derive in this work.

#### 3.8. Carbonaceous Features

The presence of extinction features arising from carbon bonds is well attested in the diffuse ISM. We review here the extinction "bump" at 2175 Å, the infrared extinction features, and the diffuse interstellar bands (DIBs).

### 3.8.1. The 2175 Å Feature

As evidenced in Figure 1, a striking feature of the interstellar extinction curve is the "bump" at 2175 Å. This feature was first discovered by Stecher (1965) and quickly identified as extinction from small graphite particles (Stecher & Donn 1965), although this identification is not universally accepted. As the backbone of a polycyclic aromatic hydrocarbon (PAH) is in many ways analogous to a graphite sheet, the 2175 Å feature may be attributable to PAHs (Donn 1968; Draine 1989a, 2003a; Joblin et al. 1992).

Regardless of the carrier of the feature, a number of observational facts appear clear. First, the feature appears ubiquitous in the ISM, found over a wide range of E(B-V) (Bless & Savage 1972; Savage 1975). Second, the feature is quite strong and therefore its carrier must be composed of one of the more abundant elements in the ISM—C, O, Mg, Si, or Fe (Draine 1989a). Third, the central wavelength of the feature is nearly invariant across many sight lines, though the width can vary dramatically (FWHM between 360 and 600 Å) across environments (Fitzpatrick & Massa 1986). Finally, this feature is weaker, and in some cases absent, in sight lines toward the LMC (Clayton & Martin 1985; Fitzpatrick 1985, 1986; Misselt et al. 1999) and SMC (Rocca-Volmerange et al. 1981; Prevot et al. 1984; Thompson et al. 1988; Gordon et al. 2003).

The consistency of the central wavelength across environments suggests that the feature is relatively insensitive to the grain size distribution, while its weakness in the SMC and LMC lends credence to the idea that it is associated with a specific carrier that may be underabundant in those environments.

While graphite-like sheets, such as those found in PAHs, provide perhaps the most attractive explanation for the feature at present, it is not without difficulties. In particular, Draine & Malhotra (1993) demonstrated that graphite has difficulty explaining the observed variations in the width of the feature by variations in the size and shape of the grains while simultaneously preserving the constant central wavelength. Alternative hypotheses, such as transitions in OH ions in amorphous silicates (Steel & Duley 1987), onion-like carbonaceous composite materials (Wada et al. 1999), and hydrogenated amorphous carbon (Mennella et al. 1998; Duley & Hu 2012), provide ways to account for the feature without invoking graphite, though most of these models still attribute the feature to carbonaceous bonds. As of yet, no hypothesis offers a clear explanation for the simultaneous near invariance of the central wavelength and substantial variation in the feature's width.

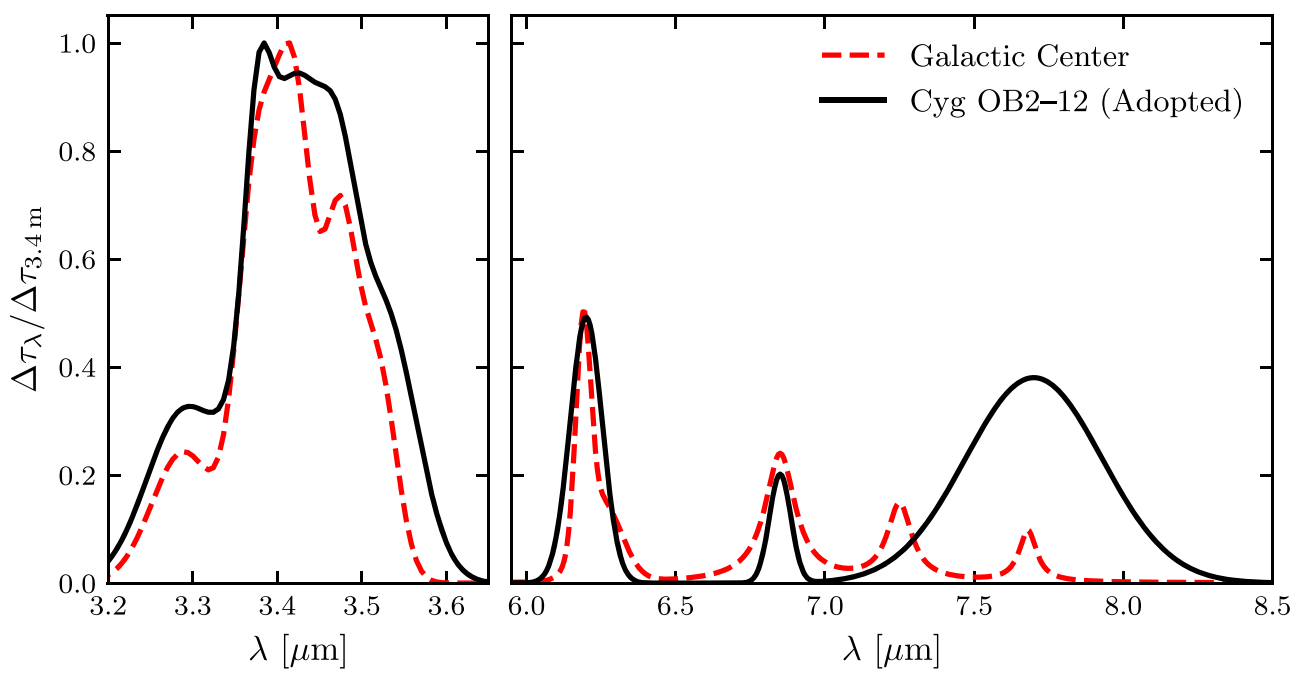


**Figure 6.** We compare determinations of the hydrocarbon feature profiles toward the Galactic Center based on ISO-SWS spectroscopy (Chiar et al. 2000, 2013) and toward Cyg OB2-12 which employed both ISO-SWS and Spitzer IRS spectroscopy (Hensley & Draine 2020). Both sets of profiles have been normalized to the maximum optical depth in the  $3.4 \mu m$  feature. Although these sight lines probe very different interstellar environments, the agreement is excellent aside from the 7.25 and  $7.7 \mu m$  features, where the determinations are most uncertain.

### 3.8.2. Infrared Features

An interstellar absorption feature at  $3.4\,\mu\mathrm{m}$  was first discovered by Soifer et al. (1976) toward the Galactic Center source IRS 7, though it was not until the nondetection of emission features at 6.2 and 7.7  $\mu\mathrm{m}$  along the same line of sight that its interstellar origin was appreciated (Willner et al. 1979). Wickramasinghe & Allen (1980) detected a pronounced  $3.4\,\mu\mathrm{m}$  feature toward IRS 7 as well as toward the M star OH 01–477, which they attributed to the CH stretch band. Detection of this feature toward Cyg OB2-12 suggests that it is a generic feature of extinction from the diffuse ISM (Adamson et al. 1990; Whittet et al. 1997).

Subsequent observations of the 3.4  $\mu$ m feature revealed a complex profile, including a number of "subpeaks" at 3.39, 3.42, and 3.49  $\mu$ m (Duley & Williams 1983; Butchart et al. 1986; Sandford et al. 1991). Sandford et al. (1991) demonstrated consistency between these features and C–H stretching in =CH<sub>2</sub> (methylene) and –CH<sub>3</sub> (methyl) groups in aliphatic hydrocarbons. These results were supported by the more extensive observations of Pendleton et al. (1994), who determined that diffuse ISM has a characteristic CH<sub>2</sub> to CH<sub>3</sub> abundance of about 2.0–2.5. Detailed comparison of the 3.4  $\mu$ m feature to laboratory measurements of a range of materials yielded a close match with hydrocarbons with both aliphatic and aromatic characteristics (Pendleton & Allamandola 2002).

A key prediction of the aliphatic hydrocarbon origin of the 3.4  $\mu$ m feature is the presence of a 6.85  $\mu$ m CH deformation mode. Tielens et al. (1996) identified this feature in an IR spectrum of the Galactic Center, confirming this hypothesis. Additionally, they identified features at 5.5 and 5.8  $\mu$ m with C=O (carbonyl) stretching and a feature at 5.5  $\mu$ m with metal carbonyls such as Fe(CO)<sub>4</sub>. Subsequently, Chiar et al. (2000) detected a 7.25  $\mu$ m feature ascribed to a methylene deformation mode toward the Galactic Center. The 6.85  $\mu$ m feature has

been observed toward Cyg OB2-12 with the same strength relative to the  $3.4\,\mu\mathrm{m}$  feature as seen toward the Galactic Center (Hensley & Draine 2020). Thus, the  $6.85\,\mu\mathrm{m}$  feature also appears generic to extinction from the diffuse ISM. On the other hand, the  $7.25\,\mu\mathrm{m}$  feature was not detected toward Cyg OB2-12, although a weak feature could not be completely ruled out. The hydrocarbon feature profiles toward the Galactic Center and Cyg OB2-12 are compared in Figure 6.

The  $3.47~\mu m$  subfeature of the  $3.4~\mu m$  complex has been attributed to bonds between H and  $sp^3$  bonded (diamond-like) C (Allamandola et al. 1992). This feature appears to be present in the spectrum of the Galactic Center (Chiar et al. 2013), and absorption in the vicinity of this feature is even stronger toward Cyg OB2-12 (Hensley & Draine 2020), as illustrated in Figure 6. While this suggests diamond-like C may be ubiquitous in both the dense and diffuse ISM, it is in conflict with the finding of Brooke et al. (1996) that the strength of the  $3.47~\mu m$  feature is better correlated with the  $3.1~\mu m$  H<sub>2</sub>O ice feature (absent toward Cyg OB2-12) than with the  $9.7~\mu m$  silicate feature. Observations of these features on more sight lines are needed to clarify the evolution of hydrocarbons in the ISM.

The attribution of the strong IR emission features to PAHs (see Section 5.2) implies the presence of aromatic features in the interstellar extinction curve in addition to the observed aliphatic features. Observing eight IR sources, including two Galactic Center sources and Cyg OB2-12, with ISO-SWS spectroscopy, Schutte et al. (1998) detected a 6.2  $\mu$ m absorption feature associated with aromatic hydrocarbons, which has a well-known corresponding emission feature. Subsequently, both the 3.3 and 6.2  $\mu$ m aromatic features were detected in absorption toward the Quintuplet Cluster (Chiar et al. 2000, 2013), and Hensley & Draine (2020) reported detections of the 3.3, 6.2, and 7.7  $\mu$ m aromatic features in absorption toward Cyg OB2-12. While there is a feature in the extinction

curve toward the Galactic Center in the vicinity of  $7.7~\mu m$ , Chiar et al. (2000) attributed it to the  $7.68~\mu m$  feature from methane ice. Because of the detection on the iceless sight line toward Cyg OB2-12, we include it in Figure 6, but note that there are substantial observational uncertainties on the depth and width of the feature in both the Galactic Center and Cyg OB2-12 determinations that may account for the difference. However, it is also possible that the discrepancy is real and that there exist fundamental differences in the relative strengths of the extinction features on these two very different sight lines. The strength of the  $7.7~\mu m$  feature detected toward Cyg OB2-12 is, however, consistent with predictions of models for interstellar PAHs (Draine & Li 2007).

While the aromatic 3.3  $\mu$ m feature is substantially weaker than the aliphatic 3.4  $\mu$ m feature in absorption, it dominates in emission. It is also noteworthy that the 3.3  $\mu$ m feature width is substantially broader in absorption ( $\Delta \lambda^{-1} \simeq 90~{\rm cm}^{-1}$ , Chiar et al. 2013; Hensley & Draine 2020) than seen in emission ( $\Delta \lambda^{-1} \simeq 30~{\rm cm}^{-1}$ , Tokunaga et al. 1991; Joblin et al. 1996).

As with the silicate features, carbonaceous features not observed in the diffuse ISM also constrain dust composition. Polycrystalline graphite is expected to have a lattice resonance in the vicinity of 11.53  $\mu$ m (Draine 1984, 2016). Such a feature was not observed toward Cyg OB2-12 (Hensley & Draine 2020), though the weakness of the feature allowed only an upper limit of <160 ppm of C in graphite to be set. More stringent upper limits will require more sensitive data and possibly a sight line without contaminating H recombination lines.

Laboratory data suggest the presence of NIR features at 1.05 and 1.23  $\mu$ m associated with ionized PAHs having 40–50 C atoms (Mattioda et al. 2005b, 2005a). These wavelengths may be too short for even ultrasmall grains to produce strong emission features, but if present, they should be observable in extinction (Mattioda et al. 2005b). However, we are unaware of any existing observational constraints on the presence or absence of these features.

### 3.8.3. The Diffuse Interstellar Bands

The diffuse interstellar bands (DIBs) are a set of numerous, relatively broad (hence "diffuse") interstellar absorption features that likely arise from molecular transitions. The first two DIBs  $\lambda5780$  and  $\lambda5795$  were noted as unidentified stellar absorption features (Heger 1922a, 1922b), but their interstellar nature was not confirmed until Merrill (1936) found that the lines remained at fixed wavelength in a spectroscopic binary while the stellar lines exhibited the expected time-dependent oscillation. Subsequently, over 500 DIBs have been identified, the vast majority of which have not been identified with a specific molecular carrier (Herbig 1995; Hobbs et al. 2009; Fan et al. 2019).

The first definitive identification of a DIB carrier did not occur until 2015 when laboratory measurements demonstrated that  $C_{60}^+$  can reproduce the absorption features at 9632 and 9577 Å (Campbell et al. 2015). Subsequent detection of the predicted 9428 Å band has confirmed  $C_{60}^+$  as the carrier (Cordiner et al. 2019). Based on the observed DIB strength, it is estimated that  $C_{60}^+$  accounts for only  $\sim 0.1\%$  of the interstellar carbon abundance (Berné et al. 2017).

The correlation between DIB strength and total reddening is nonlinear (Snow & Cohen 1974) and varies among DIBs,

suggesting that the various DIB carriers preferentially reside in different interstellar environments, e.g., atomic versus molecular gas (Lan et al. 2015). It is in principle possible to construct a representative spectrum for DIBs in diffuse H I gas assuming the empirical relations between DIB equivalent widths and  $N_{\rm H\,I}$  derived by Lan et al. (2015) for the set of 20 DIBs between 4430 and 6614 Å considered in their study, but we do not pursue such an undertaking in this work.

### 3.9. Other Features

Although we have discussed a number of extinction features associated with specific materials found in diffuse interstellar gas, this inventory is incomplete, particularly as we push to weaker features. Indeed, Massa et al. (2020) recently presented new evidence of "Intermediate Scale Structure," i.e., extinction features a few hundred to 1000 Å wide (see also York 1971), in the spectrophotometric extinction curves of Fitzpatrick et al. (2019). They identified two features at 4370 and 4870 Å, which both showed correlation with the strength of the 2175 A feature, and one feature at 6300 Å that did not. Further, they argue that the reported "Very Broad Structure" (Whiteoak 1966) is actually a minimum between the 4870 and 6300 Å features. These features affect the optical extinction at the ≤10% level, and we include them in our representative extinction curve only insofar as they are inherent in the mean extinction curves of Schlafly et al. (2016) and Fitzpatrick et al. (2019), which we employ over this wavelength range.

$$3.10. \text{ N}_{H}/\text{E(B} - \text{V)}$$

It is expected that the amount of extinction on a given sight line scales linearly with the dust column density and, to the extent that dust and gas are well mixed, with the gas column density. This scaling is borne out observationally and is typically summarized by the quantity  $N_{\rm H}/E(B-V)$ , which appears roughly constant for the diffuse ISM. Using Ly $\alpha$  absorption measurements made by the Copernicus satellite for 75 stars within 3400 pc, Bohlin et al. (1978) derived a value of  $N_{\rm H}/E(B-V)=5.8\times10^{21}~{\rm H~cm^{-2}~mag^{-1}}$ . They noted that very few of their sight lines differ from this relation by more than a factor of 1.5. Ly $\alpha$  absorption studies with IUE by Shull & van Steenberg (1985), and Diplas & Savage (1994) derived similar  $N_{\rm H~I}/E(B-V)$  values of 5.2 and 4.9 × 10<sup>21</sup> H cm<sup>-2</sup> mag<sup>-1</sup>, respectively. Finally, Rachford et al. (2009) obtained  $N_{\rm H}/E(B-V)=(5.94\pm0.37)\times10^{21}~{\rm H~cm^{-2}~mag^{-1}}$  with data from FUSE for translucent clouds ( $A_V\gtrsim0.5$ ) where both H I and H<sub>2</sub> were measured directly.

Measuring the H I column density toward globular clusters using the 21 cm line, Knapp & Kerr (1974) and Mirabel & Gergely (1979) found  $N_{\rm H\,I}/E(B-V)$  of 5.1 and 4.6  $\times$   $10^{21}$  H cm<sup>-2</sup> mag<sup>-1</sup>, respectively. These values are also consistent with data from a similar study using RR Lyrae (Sturch 1969), all of which corroborate the values from H I absorption studies.

However, employing 21 cm data from the Leiden–Argentina–Bonn (LAB) H I Survey (Kalberla et al. 2005) and the Galactic Arecibo *L*-band Feed Array (GALFA) H I Survey (Peek et al. 2011) in conjunction with the reddening map of Schlegel et al. (1998), Liszt (2014) determined  $N_{\rm HI}/E(B-V)=8.3\times10^{21}\,{\rm cm}^{-2}\,{\rm mag}^{-1}$  for  $|b|\gtrsim20^{\circ}$  and  $E(B-V)\lesssim0.1$  mag. This is a factor of 1.4 higher than that found by Bohlin et al. (1978). Liszt (2014) noted that some previous determinations

using H I emission are in good agreement with this higher value, particularly for E(B-V) < 0.1. For instance, Heiles (1976) found  $E(B-V) = (-0.041 \pm 0.012) + N_{\rm H\,I}/(4.85 \pm 0.36) \times 10^{21} \, {\rm cm}^{-2} \, {\rm mag}^{-1}$ , consistent with the higher value of Liszt (2014) when E(B-V) < 0.1 due to the negative intercept. Likewise, Mirabel & Gergely (1979) required a negative intercept to fit their data, suggesting a change in behavior at low reddening.

In a subsequent analysis, Lenz et al. (2017) correlated  $N_{\rm H\ I}$ measurements from the HI4PI Survey (HI4PI Collaboration et al. 2016) and maps of interstellar reddening as determined by Schlegel et al. (1998) over the diffuse, high-latitude sky. They found a characteristic  $N_{\rm H\,I}/E(B-V)=8.8\times10^{21}\,{\rm cm}^{-2}\,{\rm mag}^{-1}$  on these sight lines, with a systematic uncertainty of about 10%. Comparing 21 cm observations to stellar extinction along 34 sight lines with little molecular gas, Nguyen et al. (2018) found a compatible  $N_{\rm H}/E(B-V) = (9.4 \pm 1.6) \times 10^{21} \, {\rm cm}^{-2} \, {\rm mag}^{-1}$ (95% confidence interval) and that this relation persists to  $N_{\rm H}$  as high as  $3 \times 10^{21} \, {\rm cm}^{-2}$ . Using X-ray absorption to infer  $N_{\rm H}$ , Zhu et al. (2017) found a mean value of  $N_{\rm H}/A_V = (2.08 \pm 0.02) \times$ 10<sup>21</sup> toward a sample of supernova remnants, planetary nebulae, and X-ray binaries across the Galaxy. For  $R_V = 3.1$ , this corresponds to  $N_{\rm H}/E(B-V)=6.45^{\circ}\times 10^{21}\,{\rm cm}^{-2}\,{\rm mag}^{-1}$ intermediate between the Bohlin et al. (1978) and Lenz et al. (2017) values.

The striking difference between these different determinations of  $N_{\rm H}/E(B-V)$  is consistent with systematic variations of the dust-to-gas ratio in the Galaxy, with more dust per H atom in the Galactic plane and less at high Galactic latitudes. As we focus here on high-latitude sight lines where the dust emission per H atom is best determined (see Section 5), we adopt the value  $N_{\rm H}/E(B-V)=8.8\times10^{21}\,{\rm cm}^{-2}\,{\rm mag}^{-1}$  of Lenz et al. (2017) as our benchmark.

### 3.11. Scattering

Extinction is the sum of two processes—absorption and scattering. The scattering properties of dust can be constrained by studying the surface brightness profile of scattered light around point sources and the spectrum of the diffuse Galactic light. However, both of these constraints involve simultaneous modeling of both the dust optical properties and the scattering geometry and are therefore difficult to incorporate self-consistently into the present analysis. We provide a brief overview below, but do not include these observations into our final set of model constraints.

### 3.11.1. X-Ray Scattering

Interstellar grains scatter X-rays through small angles (Overbeck 1965; Hayakawa 1970; Martin 1970), which can be observed as a "scattering halo" in X-ray images of point sources with intervening interstellar dust (Catura 1983; Mauche & Gorenstein 1986). The scattering is sensitive to both dust composition and size distribution, providing additional observational constraints that a grain model should satisfy.

The angular extent of the scattering halo also depends on the location of the dust between us and the source. For Galactic sources (e.g., low-mass X-ray binaries), this introduces uncertainty when comparing models to observations.

The best-studied case is GX 13+1 (Smith 2008). Valencic & Smith (2015) surveyed 35 X-ray scattering halos and concluded that most could be satisfactorily fit by one or more dust models with size distributions having few grains larger

than  $\sim$ 0.4  $\mu$ m. Extragalactic sources with intervening Galactic dust, the exact distance to which would be unimportant, would be optimal for testing dust models, but high signal-to-noise imaging of X-ray halos around reddened AGN is lacking.

The scattering cross section for the dust grains is expected to show spectral structure near X-ray absorption edges (Draine 2003b). If this could be observed, it would provide a means to detect or constrain variations of grain composition with size. Costantini et al. (2005) reported spectral structure in the scattering halo around Cyg X-2. Features appear to be present near the O K, Fe L, Mg K, and Si K absorption edges, although the interpretation remains unclear. Future X-ray telescopes may enable more sensitive spectroscopy of scattering halos.

A population of aligned, aspherical grains can produce observable asymmetries in an X-ray scattering halo (Draine & Allaf-Akbari 2006). Seward & Smith (2013) employed Chandra observations of Cyg X-2 to search for these asymmetries, but found the X-ray halo to be uniform in surface brightness to at least the 2% level. A detection of halo asymmetry has yet to be reported.

Because X-ray scattering is sensitive to grain structure on small scales, X-ray halos can also provide constraints on grain porosity. Analyzing the Chandra observations of the Galactic binary GX 13+1 of Smith et al. (2002), Heng & Draine (2009) found that the small angle scattering from grains with porosity greater than 0.55 overpredicts the observed surface brightness in the core of the scattering halo. As the degree of compactness of interstellar grains remains a major unresolved question, ancillary data and analysis are needed to test the conclusions of Heng & Draine (2009).

### 3.11.2. Diffuse Galactic Light

Even in a dark patch of sky far from point sources, there is still light from emission from the ISM and from starlight that has been scattered off of dust grains. This "diffuse Galactic light" (DGL) was first detected in the photoelectric measurements of Elvey & Roach (1937), who derived a surface brightness of 5.6 mag per square degree at  $\lambda \approx 4500$  Å. These results were corroborated by the photometric observations of Henyey & Greenstein (1941), who concluded that dust grains must have a relatively large albedo  $\omega$  (0.3 <  $\omega$  < 0.8) and be relatively forward scattering, having anisotropy parameter  $g \equiv \langle \cos \theta \rangle$  (where  $\theta$  is the scattering angle) greater than 0.65. Particles in the Rayleigh limit (i.e., small compared to the wavelength) have  $g \approx 0$ , i.e., isotropic scattering, indicating that the scattering in the ISM is dominated by larger grains (radius  $a \gtrsim 0.1 \,\mu\text{m}$ ).

The conversion of measurements of the intensity of scattered light into constraints on the scattering properties of interstellar dust is challenging as it requires assumptions on the distribution of both sources and scatterers. Nevertheless, observations of the DGL from the optical to the UV have been used to constrain the wavelength dependence of both  $\omega$  and g.

Employing 1500–4200 Å photometric observations from the Orbiting Astronomical Observatory (OAO-2) in 71 fields at varying Galactic longitude, Lillie & Witt (1976) found good agreement with earlier ground-based measurements of the DGL. They constrained  $\omega$  and g through a radiative transfer analysis on a plane-parallel galaxy in which both dust and stars decrease exponentially with height above the disk, finding  $0.3 < \omega < 0.7$  with indications of a minimum near 2200 Å, coincident with the extinction bump (see Section 3.8.1). Except in this minimum where g attained values as high as 0.9, they found 0.6 < g < 0.7.

The UV spectrometers aboard the two Voyager spacecraft were used to study dust scattering in the Coalsack Nebula by Murthy et al. (1994). They employed a simple scattering model assuming fixed g and single scattering only to infer the wavelength dependence of the dust albedo. Fixing  $\omega=0.5$  at 1400 Å, they computed the relative albedo at other wavelengths, finding little wavelength dependence aside from a modest increase toward shorter wavelengths. A follow-up analysis by Shalima & Murthy (2004) using a more sophisticated Monte Carlo model for the dust scattering determined the FUV dust albedo to be  $0.4 \pm 0.2$ .

The Far Ultraviolet Space Telescope measured the diffuse UV continuum between 140 and 180 nm. Employing the 156 nm flux measurements from this experiment and a radiative transfer model that accounted for nonisotropic radiation fields and multiple scatterings, Witt et al. (1997) derived an FUV dust albedo of 0.45  $\pm$  0.05 and  $g=0.68\pm0.10$ . The rocket-borne Narrowband Ultraviolet Imaging Experiment for Wide-Field Surveys (NUVIEWS) measured the diffuse UV background at 1740 Å. Using a 3D Monte Carlo scattering model based on that described in Witt et al. (1997), Schiminovich et al. (2001) constrained the dust albedo to be  $\omega=0.45\pm0.05$  and  $g=0.77\pm0.1$ .

By correlating the spectra of SDSS sky fibers (i.e., spectra of the "blank" sky taken for calibration purposes) against the 100  $\mu$ m dust emission measured by IRAS, Brandt & Draine (2012) measured the spectrum of the DGL between 3900 and 9200 Å. Modeling the DGL scattering geometry with a plane-parallel exponential galaxy, they compared the observed spectrum to predictions from dust models. Their formalism could in principle be used to place constraints directly on  $\omega$  and g, but we do not pursue such analysis here.

We summarize these constraints on the dust albedo and asymmetry parameter in Figure 7. Given the modeling uncertainties inherent in translating the DGL intensity to the scattering properties of interstellar dust, we do not at this time incorporate these data into our set of constraints. These limitations notwithstanding, it is clear that interstellar dust must have a UV/optical albedo of order 0.5 and be relatively forward scattering (g > 0.5).

## 3.12. Spatial Variation of the Extinction Curve

It is well established that there is not a single universal extinction curve that describes all regions of the ISM, but rather a variety of extinction curves typically parameterized by  $R_V$ (Johnson & Borgman 1963; Cardelli et al. 1989). For instance, measurements of extinction toward the Galactic Bulge have indicated  $R_V \approx 2.5$  (Udalski 2003; Nataf et al. 2013). Schlafly et al. (2016) found large-scale gradients in  $R_V$ , with a follow-up study indicating a possible dependence on Galactocentric radius such that the outer Galaxy has a systematically higher  $R_V$  than the inner Galaxy (Schlafly et al. 2017). The magnitude of the variations in  $R_V$ , however, was relatively small ( $\sigma_{R_V} = 0.18$ , Schlafly et al. 2016). Extinction in dark clouds differs systematically from the diffuse ISM due to the growth of grains by coagulation and the formation of ice mantles. We do not attempt to summarize the observed range of variations in this work, instead restricting our focus to the extinction curve of the local diffuse ISM having an average  $R_V \approx 3.1$  (Morgan et al. 1953; Schultz & Wiemer 1975; Sneden et al. 1978; Koornneef 1983; Rieke & Lebofsky 1985; Fitzpatrick et al. 2019).

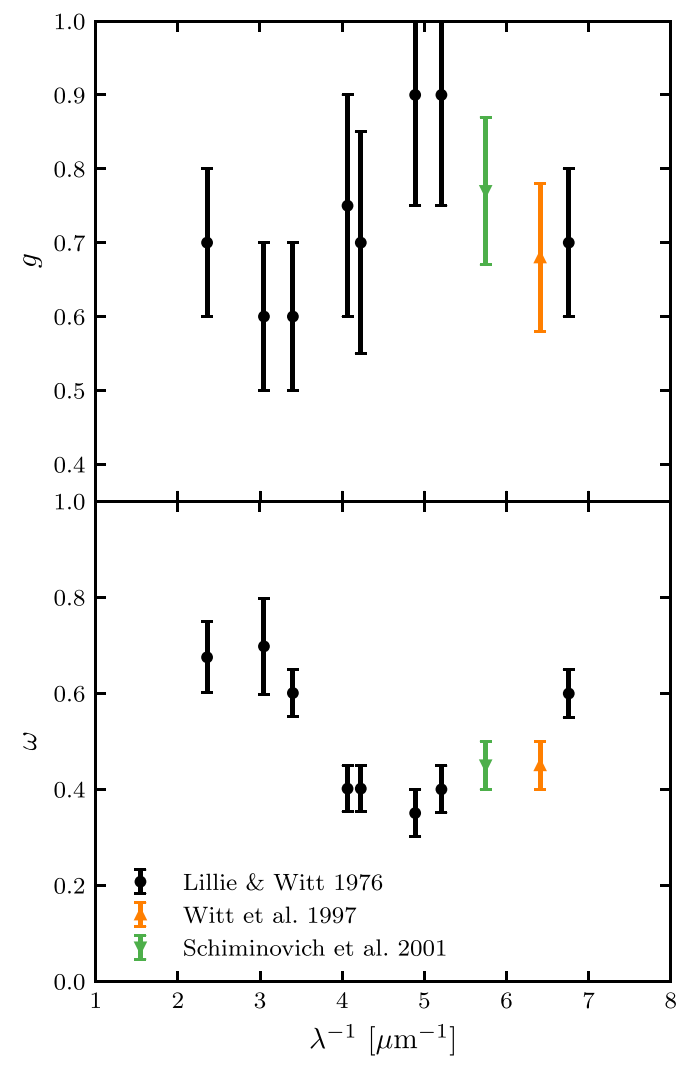


**Figure 7.** Constraints on the dust albedo  $\omega$  and phase function asymmetry  $g \equiv \langle \cos \theta \rangle$  inferred from measurements of the diffuse Galactic light.

### 4. Polarized Extinction

Following the discovery that starlight is polarized (Hall 1949; Hall & Mikesell 1949, 1950; Hiltner 1949a, 1949b, 1949c), it was quickly realized that this polarization was due to selective extinction by aligned dust grains rather than inherent polarization of the stars themselves. Davis & Greenstein (1951) proposed a physical model of grain alignment whereby aspherical dust grains were aligned by the local magnetic field. Our understanding of the alignment processes of dust grains has since undergone significant evolution (see Andersson et al. 2015, for a review), though it remains clear that observations of polarized extinction constrain the size, shape, composition, and alignment properties of interstellar dust.

In this section, we summarize observations of the polarized extinction, focusing upon its wavelength dependence, spectral features, and amplitude per unit reddening.

### 4.1. Wavelength Dependence

Initial observation of the polarized extinction from UV to NIR wavelengths (e.g., Behr 1959; Gehrels 1960, 1974; Coyne et al. 1974; Serkowski et al. 1975) established a characteristic wavelength dependence of the polarized extinction that is often

parametrized by the "Serkowski law" (Serkowski 1973):

$$p_{\lambda}/p_{\text{max}} \simeq \exp\left[-K \ln^2\left(\lambda_{\text{max}}/\lambda\right)\right],$$
 (8)

where  $p_{\lambda}$  is the polarization fraction of the two linear polarization modes and  $p_{\text{max}}$  is the maximum value of  $p_{\lambda}$  occurring at wavelength  $\lambda_{\text{max}}$ . Serkowski (1971) prescribed the values K=1.15 and  $\lambda_{\text{max}}=0.55~\mu\text{m}$ .

Subsequent observations of polarized extinction revealed that the polarization peak becomes narrower (i.e., K increases) as  $\lambda_{\rm max}$  increases (Wilking et al. 1980, 1982). This relation, known as the "Wilking law," is parametrized by the linear relationship

$$K \simeq c_1 \lambda_{\text{max}} + c_2,$$
 (9)

where  $c_1$  and  $c_2$  are constants to be fit. Analyzing the polarized extinction from the U to K band, Whittet et al. (1992) derived values of  $c_1=1.66~\mu\text{m}^{-1}$  and  $c_2=0.01$ . Employing UV polarimetry from the Wisconsin Ultraviolet Photo-Polarimeter Experiment (WUPPE), Martin et al. (1999) fit values of  $c_1=2.56~\mu\text{m}^{-1}$  and  $c_2=-0.59$ . As the former determination is a better fit to the observations from the optical to IR, and the latter a better fit from the UV to the optical, Whittet (2003) recommended a "compromise fit" employing the mean of the two determinations, i.e.,  $c_1=2.11~\mu\text{m}^{-1}$  and  $c_2=-0.29$ , yielding K=0.87 for  $\lambda_{\text{max}}=0.55~\mu\text{m}$ . For  $\lambda_{\text{max}}=0.55~\mu\text{m}$ , all three parameterizations produce a similar polarized extinction law, as shown in Figure 8.

Constraints on the polarized extinction law in the UV come almost entirely from WUPPE and the Faint Object Spectrograph on Hubble, and so while the Serkowski law appears to describe interstellar polarization down to  $\lambda \simeq 1300\,\text{Å}$  (Somerville et al. 1994), extrapolations to wavelengths shorter than were accessible by these instruments are uncertain. We therefore adopt 1300 Å as the shortest wavelength for our polarized extinction curve.

Although the Serkowski law (Equation (8)) describes well the polarized extinction in the UV and optical, it underestimates the observed polarization in the infrared, particularly between  $\sim\!2$  and 5  $\mu$ m (Jones & Gehrz 1990; Nagata 1990). Compiling determinations of the IR polarized extinction along the lines of sight to a number of molecular clouds observed by Hough et al. (1989), Martin & Whittet (1990) determined that the IR polarized extinction could be fit with a power law  $p_{\lambda} \propto \lambda^{-\beta}$  with indices ranging from  $\beta=1.5$  to 2.0. With polarimetry extending from optical wavelengths to 5  $\mu$ m, Martin et al. (1992) found the  $\sim\!1$ –4  $\mu$ m extinction was well fit by a power law with index  $\beta=1.6$ . Between 4 and 5  $\mu$ m, however, the power law systematically underpredicted the observed polarization.

The behavior of the IR polarized extinction is relatively robust to variations that exist at optical and UV wavelengths as demonstrated by Clayton & Mathis (1988).

For our representative polarized extinction curve, we adopt the "compromise fit" of Whittet (2003) with K=0.87 and  $\lambda_{\rm max}=0.55~\mu{\rm m}$  from  $0.12~\mu{\rm m}$  to the infrared. From  $\lambda=\lambda_{\rm max}\exp(\beta/2K)=1.38$  to  $4~\mu{\rm m}$ , we adopt a power law with  $\beta=1.6$ .

### 4.2. Silicate Features

If the features in the interstellar extinction curve arise from aspherical, aligned grains, then these features should also produce polarized extinction. The polarization, or lack thereof,

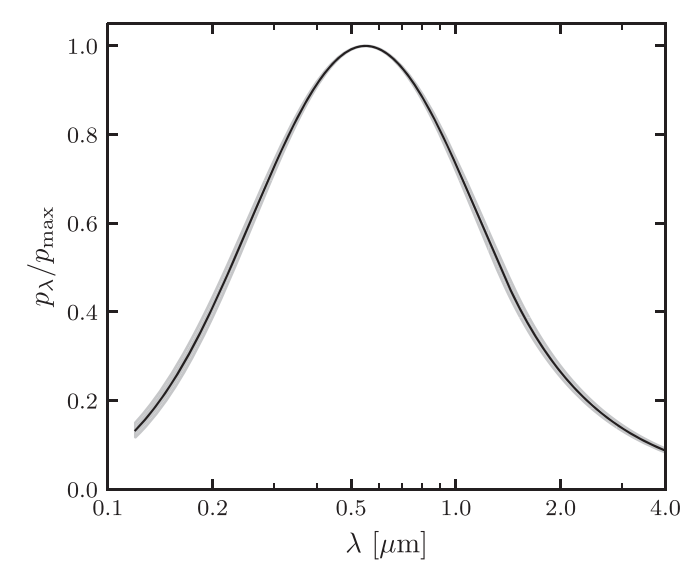


**Figure 8.** The wavelength dependence of the polarized extinction, normalized to the peak polarization. We employ the Serkowski law in the UV and optical with  $\lambda_{\rm max}=0.55~\mu{\rm m}$ , and we match this smoothly onto a power law in the IR such that  $p_{\lambda} \propto \lambda^{-1.6}$ . The solid line corresponds to a Serkowski law parameter K=0.87, while the shaded region illustrates the effects of varying K between 0.82 and 0.92, corresponding to the UV- and IR-optimized forms of the Wilking law described by Whittet (2003).

of interstellar extinction features therefore constrains the shape and alignment properties of dust of a specific composition.

The 9.7  $\mu$ m feature was first detected in polarization on the sight line toward the Becklin–Neugebauer (BN) Object in the Orion Molecular Cloud (Dyck et al. 1973; Dyck & Beichman 1974), with a detection made toward the Galactic Center soon after (Dyck et al. 1974). Subsequent observations of the BN Object have probed the frequency dependence of the polarization, including determination of the polarization profile of the 18  $\mu$ m feature (Dyck & Lonsdale 1981; Aitken et al. 1985, 1989).

Although the BN Object is well studied, its molecular environment does not likely typify the diffuse ISM. Smith et al. (2000) presented an atlas of spectropolarimetry for 55 sources between 8 and 13  $\mu$ m, and, for 6 of these, additional spectropolarimetric observations between 16 and 22  $\mu$ m. Drawing on these data, Wright et al. (2002) constructed a typical polarization profile of the 9.7  $\mu$ m silicate feature in extinction based on observations of the Wolf–Rayet stars WR 48a and WR 112. These sight lines were selected because the polarization appears dominated by interstellar absorption. However, both sight lines have H<sub>2</sub>O ice features at both 3.1 and 6.0  $\mu$ m (Marchenko & Moffat 2017) and so may differ in detail from purely diffuse sight lines. We present this composite polarization profile in Figure 9.

We are unaware of any published observations that might typify the diffuse ISM along which both  $10 \,\mu m$  and optical polarimetry have been obtained. Thus, we are unable to normalize the Wright et al. (2002) polarization profile relative to our polarized extinction curve discussed in Section 4.1.

### 4.3. Carbonaceous Features

Unlike the silicate features, the extinction features associated with carbonaceous grains have not been, with few exceptions, detected in polarization.

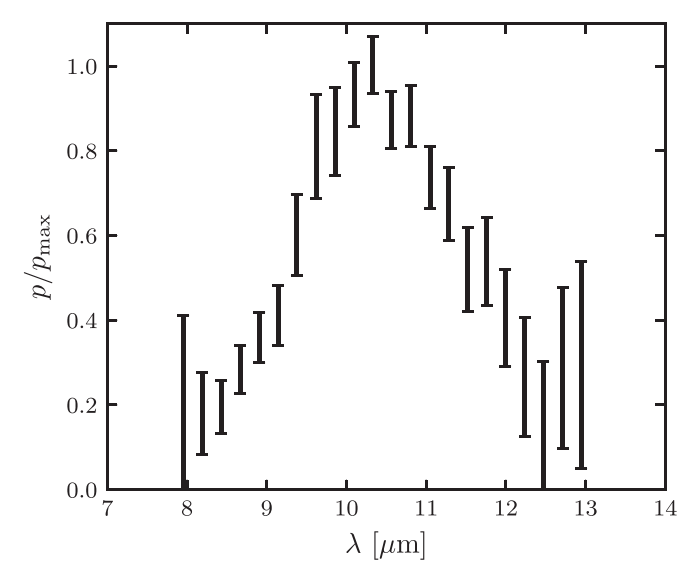


**Figure 9.** A composite polarized extinction profile of the  $9.7~\mu m$  silicate feature derived by Wright et al. (2002) from observations toward two Wolf–Rayet stars (WR 48a and WR 112). The extinction on these sight lines appears dominated by the diffuse ISM.

The 3.4  $\mu$ m feature is the strongest of the infrared extinction features associated with carbonaceous grains (see Section 3.8.2), and as such, it is a natural observational target for assessing whether carbonaceous grains give rise to polarized extinction. Low-resolution spectropolarimetric observations of five Galactic Center sources by Nagata et al. (1994) yielded no discernible polarization feature near 3.4  $\mu$ m, nor did high-resolution spectropolarimetric observations of GC-IRS 7 by Adamson et al. (1999). A subsequent search for the 3.4  $\mu$ m feature in polarization toward the young stellar object IRAS 18511+0146 likewise provided only upper limits (Ishii et al. 2002).

However, the 9.7  $\mu$ m silicate feature had not been measured along any of these sight lines, leading to ambiguity as to whether the lack of polarization was due to the carbonaceous grains themselves or the magnetic field geometry along the line of sight. This ambiguity was settled by Chiar et al. (2006), who performed spectropolarimetric observations along two lines of sight in the Quintuplet Cluster, which had existing polarimetric measurements of the silicate feature. Finding no evidence of polarization in the 3.4  $\mu$ m feature, they concluded that the carbonaceous grains responsible for the feature are much less efficient polarizers than the silicate grains. Subsequent spectropolarimetric observations of the Seyfert 2 galaxy NGC 1068 yielded no detectable feature at 3.4  $\mu$ m (Mason et al. 2007), supporting the conclusions of Chiar et al. (2006) in a markedly different interstellar environment and further challenging dust models invoking grains with silicate cores with carbonaceous mantles (see discussion in Li et al. 2014). On the basis of the nondetections reported by Chiar et al. (2006), it appears that  $\Delta p_{3.4}/\Delta p_{9.7} < 0.03$ .

The 2175 Å feature is a second natural candidate to examine for dichroic extinction arising from carbonaceous grains. Initial WUPPE results suggested excess polarization between 2000 and 3000 Å on several sight lines, with more detailed modeling suggesting that the excesses toward HD 147933-4 ( $\rho$  Oph A and B) and HD 197770 did in fact arise from the 2175 Å feature (Clayton et al. 1992; Wolff et al. 1997). However, if the 2175 Å feature had the same strength relative to the continuum polarized extinction along all lines of sight, then other

detections should have been made, e.g., toward HD 161056. The sight lines toward HD 147933-4 and HD 197770 do not betray any unusual behavior in other respects (e.g., the wavelength dependence of the polarization, the extinction curve, etc.), leading Wolff et al. (1997) to conclude that there are sight line to sight line variations in the polarizing efficiency of the grains responsible for the 2175 Å feature.

It is difficult to draw definitive conclusions on the basis of two detections (and  $\sim 30$  nondetections), emphasizing the need for more observations of UV polarization on more sight lines. Particularly now that synergy is possible with observations of FIR polarized emission, this effort promises to enhance our understanding of both grain composition and alignment.

## 4.4. Maximum $p_V/E(B-V)$

Interstellar dust grains rotate rapidly with angular momentum preferentially parallel to the local magnetic field. The short axis of each grain tends to align with the angular momentum and hence is preferentially parallel to the magnetic field. When the line of sight is parallel to the magnetic field, grain rotation eliminates any net polarization. In contrast, the polarization is greatest when the magnetic field is in the plane of the sky. Dust models should reproduce the intrinsic polarizing efficiency of dust grains, and so we focus here on the case of maximal polarization. For dust extinction, this has typically been quantified as the maximum V-band polarization per unit reddening, i.e.,  $[p_V/E(B-V)]_{\rm max}$ .

Serkowski et al. (1975) used a sample of 364 stars of various spectral types to derive  $[p_V/E(B-V)]_{\rm max}=9\%~{\rm mag}^{-1}$ . While individual stars and regions were occasionally found to have  $p_V/E(B-V)$  exceeding this upper envelope (e.g., Whittet et al. 1994; Skalidis et al. 2018), it was ambiguous whether dust on these sight lines was atypical or whether the upper envelope had been underestimated. With full-sky polarimetric measurements of dust emission, the Planck satellite facilitated a detailed comparison between polarized emission in the FIR and polarized extinction in the optical, finding a remarkably linear relation between the submillimeter polarization fraction  $p_S$  and  $p_V/E(B-V)$  (Planck Collaboration Int. XXI 2015; Planck Collaboration XII 2020, see Section 6.2). Given this relationship, the observed  $p_S \gtrsim 20\%$  in some regions implies  $p_V/E(B-V) \simeq 13\%~{\rm mag}^{-1}$ , leading Planck Collaboration XII (2020) to conclude that the classic envelope of  $9\%~{\rm mag}^{-1}$  should be revised.

Panopoulou et al. (2019) employed *R*-band RoboPol observations of 22 stars in a region with  $p_S \gtrsim 20\%$  to find that, indeed, the starlight was polarized in excess of  $p_V/E(B-V)=9\%$  mag<sup>-1</sup>, perhaps even exceeding 13% mag<sup>-1</sup>. Further, *UBVRI* polarimetry of 6 of the 22 stars indicated a typical Serkowski law in this region, suggesting that the dust on these sight lines is not atypical.

Given these recent observational results, we require that dust models reproduce  $p_V/E(B-V) = 13\% \text{ mag}^{-1}$ , and we normalize our polarization profile to this value.

# 5. Emission

In this section, we review observations of emission from interstellar dust from the infrared to microwave, focusing in particular on the emission per unit H column density characteristic of typical diffuse sight lines.

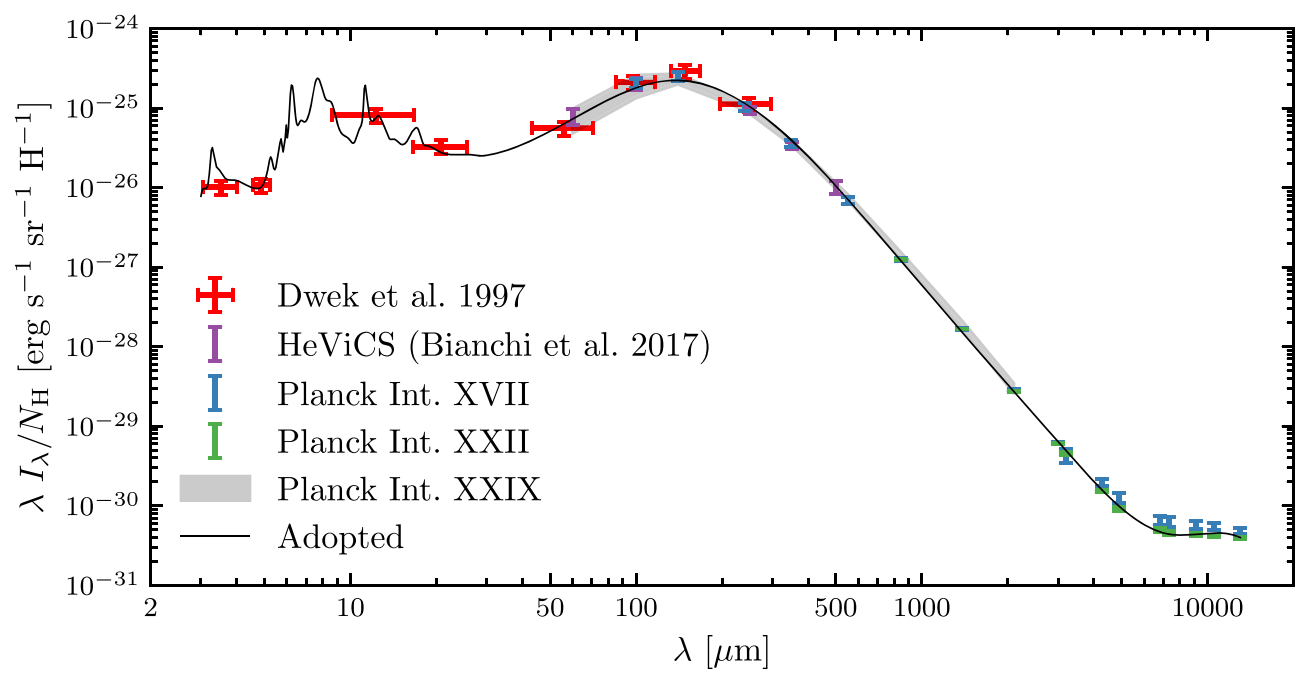


Figure 10. We plot several determinations of the H I-correlated dust emission from near-IR wavelengths through the microwave. In red is the SED of Dwek et al. (1997) derived from DIRBE data, in purple the determination of Bianchi et al. (2017) using Herschel and IRAS data, and in blue the SED of Planck Collaboration Int. XVII (2014), which employs DIRBE, WMAP, and Planck data. The horizontal bars on the DIRBE data indicate the bandpasses. We plot in gray a range of dust SEDs per  $A_V$  from Planck Collaboration Int. XXIX (2016), which we have renormalized to the hydrogen column (see text), and in green a dust SED based on correlations with the 353 GHz emission (Planck Collaboration Int. XXII 2015). The anomalous microwave emission (AME) is evidenced by the flattening of the SED at wavelengths  $\lambda \gtrsim 6$  mm.

### 5.1. IR Emission

In radiation fields typical of the diffuse ISM, the bulk of the dust grains are heated to  $\sim 20$  K and therefore emit thermally in the FIR. These wavelengths are largely inaccessible from the ground, necessitating balloon- and space-based observations.

The DIRBE and FIRAS instruments aboard the Cosmic Background Explorer (COBE) constrained the spectrum of the diffuse ISM from 3.5 to  $1000~\mu m$ . In addition to confirming the presence of PAH emission near 3.5 and  $4.9~\mu m$ , Dwek et al. (1997) derived the H I-correlated spectral energy distribution (SED) of dust in the diffuse ISM. We plot this SED in Figure 10. We note that these data were color-corrected assuming a source spectrum with constant  $\lambda I_{\lambda}$  across the band.

Prior to the release of the Planck dust maps, several studies synthesized the existing data from COBE and WMAP to produce self-consistent dust SEDs. Paradis et al. (2011) extracted an area of the sky with  $|b| > 6^{\circ}$  and an FIRAS 240  $\mu$ m intensity greater than 18 MJy sr<sup>-1</sup>, corresponding to a sky fraction of 13.7%. Compiègne et al. (2011), also seeking a composite dust SED in which the emission in each band was determined over the same region of the sky, combined DIRBE, FIRAS, and WMAP observations at high Galactic latitudes ( $|b| > 15^{\circ}$ ) and low H I column densities ( $N_{\rm H\,I} < 5.5 \times 10^{20} \, {\rm cm}^{-2}$ ). The differences between these SEDs and that of Dwek et al. (1997) are minor at their overlapping wavelengths.

The Planck satellite made sensitive measurements of the FIR-submillimeter dust emission over the full sky. Combining the Planck data with WMAP and DIRBE and correlating with H I emission measured by the Parkes 21 cm survey, Planck Collaboration Int. XVII (2014) constructed a mean SED of the diffuse ISM ( $N_{\rm H\,I}\sim3\times10^{20}\,{\rm cm}^{-2}$ ) from infrared to microwave wavelengths, which we plot in Figure 10. Following Planck Collaboration Int. XXII (2015), we apply a correction of

1.9%, -2.2%, and -3.5% to the 353, 545, and 857 GHz bands, respectively, due to updates in the Planck bandpass determinations subsequent to the work of Planck Collaboration Int. XVII (2014), and an additional 1.5% upward correction to the 353 GHz band following Planck Collaboration XI (2020). We color-correct these data using the tables in Planck Collaboration Int. XVII (2014) to express the SED in terms of monochromatic intensities at the reference frequencies and thus facilitate direct comparison to models.

Recently, Planck Collaboration Int. LVII (2020) correlated the Planck 545 GHz dust amplitude maps from the NPIPE data-processing pipeline with H I4PI maps (HI4PI Collaboration et al. 2016) filtered to retain only H I velocities between  $\pm 90~\rm km~s^{-1}$  (Lenz et al. 2017). They found  $\lambda I_{\lambda}/N_{\rm H}=7.74\times 10^{-27}~\rm erg~s^{-1}~sr^{-1}~H^{-1}$  at 545 GHz, slightly higher than but consistent with the value from Planck Collaboration Int. XVII (2014) quoted in Table 3.

The use of H I correlation to separate the Galactic dust emission from other components becomes increasingly unreliable at low frequencies where these other components, such as free–free and synchrotron, can have nonzero correlation with H I. Planck Collaboration Int. XXII (2015) derived a microwave dust SED by correlating emission in the lower frequency Planck bands with the 353 GHz emission. We plot this SED in Figure 10. While this SED and the H I-based SED of Planck Collaboration Int. XVII (2014) agree very well from 353 to 94 GHz, they diverge at lower frequencies.

There is evidence that the shape of the dust SED is not uniform across the sky and indeed varies systematically with the strength of the radiation field that heats the dust. Planck Collaboration Int. XXIX (2016) explored this relationship by fitting the dust model of Draine & Li (2007) to full-sky maps of infrared dust emission. They then normalized these SEDs to the

Table 3
Infrared Dust Emission per H

ν (GHz)	$({\rm erg}\ {\rm s}^{-1}{\rm sr}^{-1}{\rm H}^{-1})$	$(\lambda P_{\lambda}/N_{\rm H})_{\rm max}$ (erg s <sup>-1</sup> sr <sup>-1</sup> H <sup>-1</sup> )
3000	$(2.05 \pm 0.29) \times 10^{-25}$	
2140	$(2.51 \pm 0.30) \times 10^{-25}$	
1250	$(1.05 \pm 0.12) \times 10^{-25}$	
857	$(3.49 \pm 0.36) \times 10^{-26}$	
545	$(6.78 \pm 0.73) \times 10^{-27}$	
353	$(1.281 \pm 0.015) \times 10^{-27}$	$(2.514 \pm 0.030) \times 10^{-28}$
217	$(1.698 \pm 0.016) \times 10^{-28}$	$(3.407 \pm 0.054) \times 10^{-29}$
143	$(2.798 \pm 0.038) \times 10^{-29}$	$(5.68 \pm 0.10) \times 10^{-30}$
100	$(6.18 \pm 0.13) \times 10^{-30}$	$(1.174 \pm 0.031) \times 10^{-30}$
94	$(4.66 \pm 0.22) \times 10^{-30}$	
70.4	$(1.544 \pm 0.050) \times 10^{-30}$	$(2.42 \pm 0.19) \times 10^{-31}$
61	$(9.25 \pm 0.62) \times 10^{-31}$	
44.1	$(5.08 \pm 0.27) \times 10^{-31}$	$(4.06 \pm 0.74) \times 10^{-32}$
41	$(4.66 \pm 0.24) \times 10^{-31}$	
33	$(4.41 \pm 0.17) \times 10^{-31}$	
28.4	$(4.25 \pm 0.15) \times 10^{-31}$	
23	$(4.05 \pm 0.13) \times 10^{-31}$	

**Note.** Adopted dust SED per H and maximum polarized SED per H for the high-latitude diffuse ISM. These SEDs are based on those presented in Planck Collaboration Int. XVII (2014), Planck Collaboration Int. XXII (2015), and Planck Collaboration XI (2020), and have been color-corrected (see Section 5.1).

observed optical extinction based on SDSS observations of more than 250,000 quasars.

At 353 GHz, the median SED has an intensity per  $A_V$  of 0.92 MJy sr<sup>-1</sup> mag<sup>-1</sup>, while Planck Collaboration Int. XVII (2014) measured a 353 GHz intensity per hydrogen of  $3.9 \times 10^{-22}$  MJy sr<sup>-1</sup> cm<sup>2</sup> H<sup>-1</sup>. Taking these at face value implies  $A_V/N_{\rm H}=4.2\times 10^{-22}$  mag cm<sup>2</sup>. In contrast, from our adopted  $N_{\rm H}/E(B-V)=8.8\times 10^{21}\,{\rm cm}^{-2}\,{\rm mag}^{-1}$  (see Section 3.10) and  $R_V=3.1$  (see Section 3.4), we compute  $A_V/N_{\rm H}=3.5\times 10^{-22}\,{\rm cm}^2$  mag. Green et al. (2018) found that the Planck Collaboration XI (2014) reddening map calibrated on SDSS quasars overpredicted stellar reddenings by a factor of ~1.25 at intermediate latitudes, suggesting these discrepancies are rooted in the reddening calibration. We therefore correct the SEDs per  $A_V$  of Planck Collaboration Int. XXIX (2016) upward by 25% when comparing them to other determinations.

In Figure 10, we plot the range of dust SEDs over different values of the radiation field strength from Planck Collaboration Int. XXIX (2016). While there are expected systematic variations in the individual SEDs, the range is consistent with the other determinations within the uncertainties. The systematic variations of the dust SED with the radiation field may encode information about the evolution of dust properties in different environments (Fanciullo et al. 2015).

A final recent determination of the FIR dust emission comes from the Herschel satellite. Bianchi et al. (2017) correlated data from the Herschel Virgo Cluster Survey (HeViCS) with HI emission data from the Arecibo Legacy Fast ALFA (ALFALFA) Survey over a small patch of sky (76 deg²) over the Virgo cluster. Despite analyzing only 0.2% of the sky, they find excellent agreement with the Planck Collaboration Int. XVII (2014) spectrum derived over 7500 deg². We include the HeViCS spectrum in Figure 10.

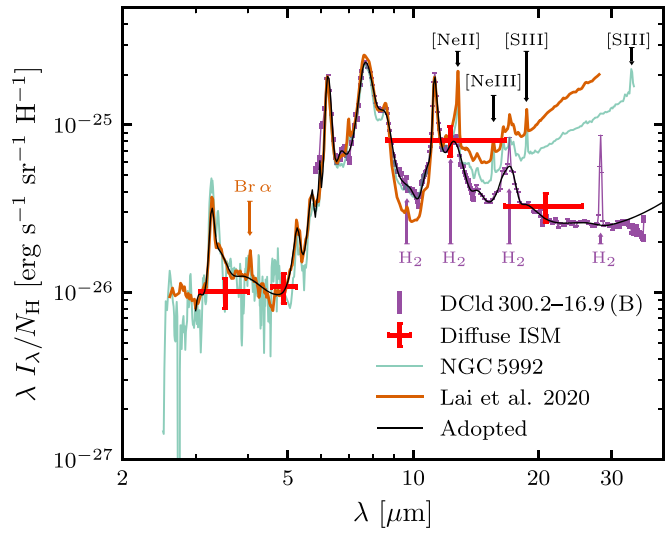


**Figure 11.** In violet, we plot the Spitzer IRS spectrum of the translucent cloud DCld 300.2–16.9 (B) as determined by Ingalls et al. (2011), where we have noted the locations of rotational  $\rm H_2$  lines. In green, we plot the combined Spitzer and AKARI spectrum of the star-forming SBb galaxy NGC 5992 (Brown et al. 2014), and in orange, we plot the average Spitzer and AKARI spectrum of PAH-bright galaxies (Lai et al. 2020). Both have been corrected for starlight emission by subtraction of a 5000 K blackbody. We indicate the strong emission lines present in the spectra. In red, we plot the H I-correlated dust emission as seen by DIRBE (Dwek et al. 1997), which we use to normalize the PAH emission spectra.

We adopt as a dust model constraint the dust SED of Planck Collaboration Int. XVII (2014) based on H I correlation from the 100, 140, and 240  $\mu$ m DIRBE bands, which overlap with the SED of Dwek et al. (1997), down to the 353 GHz Planck band. Given the known issues with H I correlation at low frequencies, we adopt the SED of Planck Collaboration Int. XXII (2015) from the Planck 217 GHz band to the WMAP 23 GHz band, normalizing to the measured 353 GHz intensity per H atom derived by Planck Collaboration Int. XVII (2014). At the lowest frequencies, the dust emission is dominated by the AME, which we discuss in Section 5.3. Our adopted dust SED is presented in Table 3, where we have color-corrected all data to facilitate direct comparisons to models.

### 5.2. Infrared Emission Features

The mid-IR emission from dust is characterized by prominent emission features at 3.3, 6.2, 7.7, 8.6, 11.3, 12.0, 12.7, 13.55, and 17  $\mu$ m (see Figures 10 and 11). First observed in the 1970s (e.g., Gillett et al. 1973; Merrill et al. 1975), these features were subsequently identified as vibrational modes of PAHs (Leger & Puget 1984; Allamandola et al. 1985). As grains must be heated to quite high temperatures in order to excite these modes ( $T \gtrsim 250$  K), the carriers must be small enough to be heated through the absorption of a single photon. This process can bring small grains to temperatures in excess of 1000 K.

The width and ubiquity of these emission features make it implausible that they are due to a single species of PAH. Rather, they represent the aggregate emission from a diverse population of PAH-like molecules. The 3.3  $\mu$ m feature, also observed in extinction (see Section 3.8.2), has been identified with the aromatic C–H stretching mode; C–C stretching modes account for the 6.2 and 7.7  $\mu$ m features, which have also been observed in extinction (see Section 3.8.2); the C–H in-plane

bending mode gives rise to the 8.6  $\mu$ m feature, while the C–H out-of-plane bending mode produces the 11.3, 12.0, 12.7, and 13.5  $\mu$ m features depending on whether one, two, three, or four hydrogen atoms are adjacent, respectively. A detailed summary of the features and their corresponding modes can be found in Allamandola et al. (1989) and Tielens (2008).

The strength of these features suggests that a substantial amount of interstellar carbon must reside in the grains giving rise to this emission. The dust model of Draine & Li (2007) required 4.7% of the total dust mass to reside in PAHs with fewer than  $10^3$  carbon atoms, which accounted for  $\sim 10\%$  of the total interstellar carbon abundance.

In addition to aromatic features associated with PAHs, the aliphatic  $3.4~\mu m$  feature has also been observed in emission (e.g., Geballe et al. 1985; Sloan et al. 1997; Lai et al. 2020), though it is typically much weaker than the  $3.3~\mu m$  aromatic feature. Comparing the strengths of these two features and assuming the  $3.4~\mu m$  feature arises solely from aliphatic carbon, Li & Draine (2012) concluded that no more than about 10% of the carbon in grains giving rise to these emission features can be in an aliphatic bond. However, it should be noted that anharmonicity in the aromatic  $3.3~\mu m$  C–H stretching mode may also contribute to the emission at  $3.4~\mu m$  (Barker et al. 1987; Li & Draine 2012), further reducing the abundance of the aliphatic component.

Using Spitzer IRS, Ingalls et al. (2011) made spectroscopic measurements between 5.2 and 38  $\mu$ m of several regions in the translucent cloud DCld 300.2–16.9. In addition to featuring IR H<sub>2</sub> transitions, these measurements provide a reasonable proxy for the PAH emission in the diffuse ISM. We plot the spectrum of their sight line "B" in Figure 11, where we have noted the observed H<sub>2</sub> lines. If a column density of  $3.9 \times 10^{21}$  cm<sup>-2</sup> is assumed, the bandpass-integrated SED agrees well with the H I-correlated DIRBE SED of the diffuse ISM as determined by Dwek et al. (1997; see Section 5.1). <sup>12</sup>CO observations of this cloud suggest N (H<sub>2</sub>)  $\sim 2 \times 10^{21}$  cm<sup>-2</sup> (Ingalls et al. 2011), and so this column density appears reasonable.

Combining spectroscopy from Spitzer and AKARI, along with ancillary data from the UV to the IR, Brown et al. (2014) presented an atlas of 129 galaxy SEDs spanning a range of galaxy types. We focus on their 2.5–34  $\mu$ m spectrum of NGC 5992, a star-forming SBb galaxy. To remove the continuum emission from starlight in this spectrum, we subtract a 5000 K blackbody component. We also note the presence of some emission lines in the spectrum arising from H II regions: [Ne II] at 12.81  $\mu$ m and [S III] at 12.81 and 18.71  $\mu$ m. In Figure 11, we compare the MIR spectra of DCld 300.2–16.9 (B) and NGC 5992, finding excellent agreement between  $\simeq$ 5 and 12  $\mu$ m.

More recently, Lai et al. (2020) presented a synthesis of combined AKARI and Spitzer spectra of star-forming galaxies. In Figure 11, we plot their "1C" spectrum, corresponding to galaxies that are PAH-bright but excluding active galactic nuclei. As with the NGC 5992 spectrum, we subtract a 5000 K blackbody component such that the shape of the spectrum is in rough agreement with both NGC 5992 and DCld 300.2–16.9 (B) in regions of overlap, but averaging over many galaxies and an improved treatment of the region of spectral overlap between AKARI and Spitzer reveal several features not readily apparent in the NGC 5992 spectrum, in particular the  $5.3 \, \mu m$ 

PAH complex and the subdominant but distinct feature at 3.4  $\mu$ m.

As the AKARI data constrain the PAH emission at short wavelengths, we adopt the SED of Lai et al. (2020) as our benchmark between 3 and 12  $\mu$ m. Given the uncertainty of the starlight subtraction, we do not employ the data at wavelengths less than 3  $\mu$ m. The spectra of Lai et al. (2020) and DCld 300.2–16.9 diverge beyond 12  $\mu$ m, likely due to the more intense starlight heating, and consequently higher temperature grains, in the sample of PAH-bright galaxies. The spectrum of DCld 300.2–16.9 is more likely to typify the diffuse ISM and is in good agreement with the shape of the DIRBE SED, and thus we adopt it as our benchmark from 12–38  $\mu$ m. However, we excise portions of the spectrum in the vicinity of the S(0), S(1), and S(2) H<sub>2</sub> rotational transitions at 28.2, 17.0, and 12.3  $\mu$ m, respectively.

In addition to the hydrocarbon features discussed above, weak MIR emission features from the C–D stretching modes of deuterated aromatic and aliphatic hydrocarbons are expected near 4.5  $\mu$ m, given that in the diffuse ISM, D is often substantially depleted from the gas phase (Linsky et al. 2006). Detections of such emission features have been reported (Peeters et al. 2004; Doney et al. 2016), but interpretation remains uncertain.

### 5.3. Anomalous Microwave Emission

The AME was discovered as a dust-correlated emission component in the microwave, both in COBE maps at 31.5, 53, and 90 GHz (Kogut et al. 1996; de Oliveira-Costa et al. 1997) and observations of the North Celestial Pole made with the Owens Valley Radio Observatory 5.5 m telescope at 14.5 and 32 GHz (Leitch et al. 1997). While these studies suggested free–free emission as a possible explanation, Draine & Lazarian (1998) argued against this interpretation on energetic grounds and suggested instead that electric dipole emission from spinning ultrasmall grains was the responsible mechanism. For a recent review of AME, see Dickinson et al. (2018).

The Perseus Molecular Cloud is perhaps the best-studied AME source and the excellent frequency coverage near the AME peak helps constrain the underlying SED. It exhibits a pronounced emission peak near 30 GHz with a sharp decline to both higher and lower frequencies (see Génova-Santos et al. 2015 for a compilation of low-frequency observations of Perseus).

The AME of the diffuse ISM appears systematically different than what has been observed in specific clouds. For instance, the AME SED derived from all-sky WMAP and Planck maps does not exhibit a low-frequency turnover but rather has a spectrum that appears to rise through the lowest frequency band (WMAP 23 GHz; Miville-Deschênes et al. 2008; Planck Collaboration X 2016). However, C-BASS observations in the North Celestial Pole region indicate no presence of diffuse AME at 5 GHz (Dickinson et al. 2019). More data between 5 and 23 GHz are required to place constraints on the AME SED of the diffuse ISM, in particular its peak frequency.

The SED of dust-correlated emission derived by Planck Collaboration Int. XXII (2015) and presented in Table 3 includes an AME component at microwave frequencies, as can be seen in Figure 10. However, the 353 GHz emission is not perfectly correlated with AME in general (e.g., Planck Collaboration Int. XV 2014; Hensley et al. 2016; Planck

Collaboration XXV 2016; Dickinson et al. 2019), and so a correlation analysis may underestimate the amount of AME relative to the submillimeter dust emission. Additionally, the other low-frequency foregrounds like free–free and synchrotron emission are also dust-correlated (Choi & Page 2015; Krachmalnicoff et al. 2018), which may bias the shape of the derived AME SED.

Parametric component separation with the Commander code has yielded full-sky maps of AME (Planck Collaboration X 2016) and mitigates some of the concerns with a correlation-based approach. Employing these maps over the full sky, Planck Collaboration XXV (2016) found the ratio of specific intensities  $I_{\nu}$  of the 22.8 GHz AME to the 100  $\mu \rm m$  and 545 GHz dust emission to be (3.5  $\pm$  0.3)  $\times$  10<sup>-4</sup> and (1.0  $\pm$  0.1)  $\times$  10<sup>-3</sup>, respectively. When instead restricting to  $|b| > 10^{\circ}$ , consistent results are obtained to within the uncertainties. This agrees reasonably well with the Planck Collaboration Int. XXII (2015) SED, which has corresponding ratios of 2.6  $\times$  10<sup>-4</sup> and 1.1  $\times$  10<sup>-3</sup>, respectively.

Given this agreement, we take the SED of Planck Collaboration Int. XXII (2015) as representative even at AME-dominated wavelengths. However, we note that the AME varies both in intrinsic strength and peak frequency from region to region (Planck Collaboration Int. XV 2014; Planck Collaboration XXV 2016), so comparisons between dust models and an average SED should be made with care.

### 5.4. Luminescence

In addition to scattering optical light, dust grains also luminesce—emit optical photons following absorption of a higher energy photon. This can be the result of fluorescence—radiative deexcitation of the excited electronic level produced by absorption. Alternatively, internal conversion may lead to the excitation of a different electronically excited state that then deexcites radiatively, a process termed "Poincaré fluorescence" (Leger et al. 1988).

Luminescence at extreme red wavelengths (6000–8000 Å, corresponding to  $1.5 \lesssim h\nu \lesssim 2.1$  eV) has been observed in a number of reflection nebulae, including the well-studied objects NGC 2023 and NGC 7023 (Witt & Boroson 1990). Because the emission is spatially extended, it is referred to as "extended red emission" (ERE; Witt et al. 1984b). ERE is also seen in some planetary nebulae (Furton & Witt 1990, 1992), and in some unusual systems such as the Red Rectangle (Cohen et al. 1975; Schmidt et al. 1980), where it was first discovered. The dust in reflection nebulae is presumed to be interstellar dust that happens to be illuminated by a nearby star, and so we expect ERE to be a property of the general interstellar dust population.

ERE is present in carbon-rich planetary nebulae but has not been observed in oxygen-rich planetary nebulae. This strongly suggests that carbonaceous material is responsible for the ERE (Witt & Vijh 2004). In reflection nebulae, ERE is seen only when the exciting star has  $T_{\rm eff} > 10,000~{\rm K}$ , hot enough to provide ample far-UV radiation (Darbon et al. 1999). From the spatial distribution in IC 59 and IC 63, Lai et al. (2017) argue that ERE is excited by  $11 < h\nu < 13.6~{\rm eV}$  far-UV photons. Observed ERE intensities in reflection nebulae indicate overall photon conversion efficiencies (ERE photons emitted per UV photon absorbed) of  $\lesssim 1\%$  (Smith & Witt 2002).

A number of authors have reported detection of the ERE from dust in Galactic cirrus clouds in the general ISM (Guhathakurta & Tyson 1989; Gordon et al. 1998; Szomoru & Guhathakurta 1998; Witt et al. 2008). Gordon et al. (1998)

estimated the ERE emissivity to be

$$\frac{\text{ERE photons}}{\text{H atoms}} = 5.65 \times 10^{-14} \frac{\text{photons}}{\text{s H atom}}$$
 (10)

with a required quantum yield of  $10\% \pm 3\%$  if the ERE is excited by absorbed photons in the  $2.25{\text -}13.6\,\text{eV}$  range. While certain materials do indeed have high quantum efficiencies (e.g., multilayer structures of  $\text{SiO}_{0.9}/\text{SiO}_2$  luminesce at  $\sim\!0.9\,\mu\text{m}$  with a quantum yield of  $\sim\!45\%$ ; Valenta et al. 2019), an overall yield of 10% would strongly constrain candidate grain materials.

Furthermore, if the ERE is actually primarily excited by 11–13.6 eV photons, as concluded by Lai et al. (2017), then the ERE intensities reported by Gordon et al. (1998) would require an overall quantum yield approaching 100%. This would require that (1) the ERE must originate from a major grain component, one accounting for a substantial fraction of the far-UV absorption, and (2) this component must have a quantum efficiency of order 100% for emitting an ERE photon following an FUV absorption. We are not aware of any candidate grain materials that could meet this requirement while complying with elemental abundance constraints, and the observed extinction properties of interstellar dust.

On the other hand, measurement of the 4000–9000 Å spectrum of the diffuse Galactic light using SDSS blank sky spectra found that the shape of the diffuse light spectrum was consistent with the scattered light expected for standard grain models (Brandt & Draine 2012). Brandt & Draine (2012) estimated that no more than  $\sim\!10\%$  of the dust-correlated diffuse light at  $\sim\!6500$  Å could be ERE. This upper limit is inconsistent with the claimed detections toward individual cirrus clouds (Guhathakurta & Tyson 1989; Gordon et al. 1998; Szomoru & Guhathakurta 1998). Additional observations will be needed to resolve this conflict.

We will assume that dust in both reflection nebulae and the general ISM produces ERE when illuminated by 11 eV  $\lesssim h \nu <$  13.6 eV photons, with an overall photon conversion efficiency  $\sim$ 1% as seen in bright reflection nebulae. This conversion efficiency could either be the result of a low conversion efficiency for a major dust component or high conversion efficiency emission from a minor dust component (e.g., elements of the PAH population).

In addition to the ERE, there is evidence for luminescence in the blue, peaking near  $\sim\!\!3750\,\mathring{A},$  in the Red Rectangle (Vijh et al. 2004), and in four reflection nebulae (Vijh et al. 2005). Vijh et al. (2004) suggested that the emission is fluorescence in small, neutral PAHs, containing three to four rings, such as anthracene (C14H10) and pyrene (C16H10). It is not clear what abundance would be required to account for the blue luminescence.

### 6. Polarized Emission

In this section, we review observations of polarized infrared emission from interstellar dust and its connection to the observed polarized extinction.

### 6.1. Infrared Emission

Just as aligned, aspherical grains polarize the starlight they absorb, the infrared emission from this same population of grains will be polarized.

The balloon-borne Archeops experiment (Benoît 2002) provided a first look at polarized dust emission from the

diffuse ISM in the Galactic plane. The 353 GHz observations indicated polarization fractions of 4%–5%, with values exceeding 10% in some clouds (Benoît et al. 2004), suggesting substantial alignment of the grains providing the submillimeter emission.

WMAP produced full-sky polarized intensity maps from 23 to 93 GHz. Utilizing the final 9 yr WMAP data, Bennett et al. (2013) found that the polarized dust emission  $P_{\nu}$  in the WMAP bands is well fit by a power law  $P_{\nu} \propto \nu^{2+\beta}$  with  $\beta=1.44$ .

With polarimetric observations extending from 30 to 353 GHz, the Planck satellite provided unprecedented constraints on the frequency dependence of the polarized emission. Planck Collaboration Int. XXII (2015) found that the full-sky average of the polarized intensity of the dust emission from 100 to 353 GHz is consistent with a modified blackbody having power-law opacity  $\kappa_{\nu} \propto \nu^{\beta}$  with  $\beta = 1.59 \pm 0.02$  in contrast with  $\beta = 1.51 \pm 0.01$  for total intensity over the same frequency range. This would imply a decrease in the polarization fraction between 353 and 70.4 GHz with a significance greater than  $3\sigma$ .

Subsequently, Planck Collaboration XI (2020) employed the SMICA component separation algorithm to derive a global polarized dust SED. Despite making no assumptions on the parametric form of the dust SED, they found excellent agreement with a modified blackbody having  $T_d=19.6~{\rm K}$  and  $\beta=1.53\pm0.02$ . Following updates to the Planck photometric calibration, they revised the  $\beta$  for total intensity to 1.48. With these changes, the  $\beta$  determined for intensity and polarization are the same within  $2\sigma$ . In Figure 12, we plot the polarized dust SED of Planck Collaboration XI (2020) and adopt it as a model constraint. We discuss the normalization of this SED to the hydrogen column in Section 6.2.

In addition to these large-scale observations of the diffuse ISM, polarimetric observations of dense clouds have also shed light on the FIR polarization properties of interstellar dust. In star-forming molecular clouds, the degree of polarization has been observed to fall from 60 to 350  $\mu$ m, then rise from 350 to 450  $\mu$ m (Vaillancourt 2002; Vaillancourt et al. 2008). This behavior can potentially be explained by correlated variations in the dust temperature and alignment efficiency in different regions along the line of sight, as might be expected in star-forming dense clouds.

However, BLASTPol observations of the Vela C molecular cloud region and the Carina Nebula have revealed very little ( $\lesssim 10\%$ ) evolution in the dust polarization fraction between 250 and 850  $\mu$ m (Gandilo et al. 2016; Ashton et al. 2018; Shariff et al. 2019). In particular, Ashton et al. (2018) studied translucent sight lines in the Vela Molecular Ridge, which is more likely to resemble diffuse sight lines than the observations at higher column densities. We present their determination of the dust polarization fraction, normalized to unity at 353 GHz, in Table 4 alongside the polarization fractions implied by the polarized dust SED of Planck Collaboration XI (2020) presented in Table 3.

Taken together, the Planck and BLASTPol results suggest a roughly constant dust polarization fraction between  $250 \,\mu\text{m}$  and 3 mm, as shown in Figure 13.

Because very small nanoparticles are not expected to be aligned (Draine & Hensley 2016), polarization in the MIR dust emission features is generally not expected due to the small sizes of the grains able to emit at these wavelengths. However, a detection of polarization in the 11.3  $\mu$ m PAH feature has been reported in the

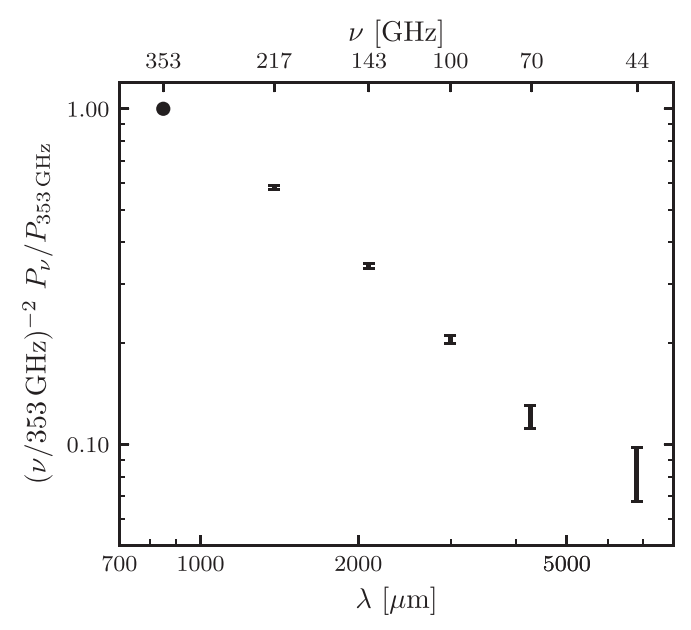


**Figure 12.** The submillimeter polarized dust SED as determined from the SMICA component separation algorithm on Planck polarization data (Planck Collaboration XI 2020). The normalization of this SED to the hydrogen column is discussed in Section 6.2.

**Table 4**Dust Polarization Fraction

$\lambda$	$p(\nu)/p_{353}$
$(\mu m)$	
250	$1.00 \pm 0.09$
350	$1.06 \pm 0.11$
500	$0.89 \pm 0.09$
850	1.0
1382	$1.02 \pm 0.03$
2100	$1.03 \pm 0.03$
3000	$0.98 \pm 0.04$
4260	$0.80\pm0.07$
6800	$0.13 \pm 0.03$

**Note.** The dust polarization fraction relative to  $850 \, \mu m$  (353 GHz) as determined from BLASTPol observations in the Vela Molecular Ridge (Ashton et al. 2018) and the Planck total and polarized dust SEDs (Planck Collaboration Int. XVII 2014; Planck Collaboration Int. XVII 2015; Planck Collaboration XI 2020) compiled in Table 3.

nebula associated with the Herbig Be star MWC 1080 (Zhang et al. 2017). If the polarization is indeed resulting from aligned PAHs, this may have implications for the theory of alignment of ultrasmall grains and thus predictions of AME polarization (Draine & Hensley 2016; Hoang & Lazarian 2018). However, it is not clear that either the dust properties or physical conditions in this region are likely to typify the diffuse ISM, and so we do not employ this result as a dust model constraint.

### 6.2. Connection to Optical Polarization

Because the same grains are believed to provide both polarized extinction in the optical and polarized emission in the infrared, it is expected that these quantities should be tightly related. Indeed, the polarization fraction of the 353 GHz submillimeter emission  $p_{353}$  divided by the V-band polarization per optical depth  $p_V/\tau_V$  has a characteristic value between 4

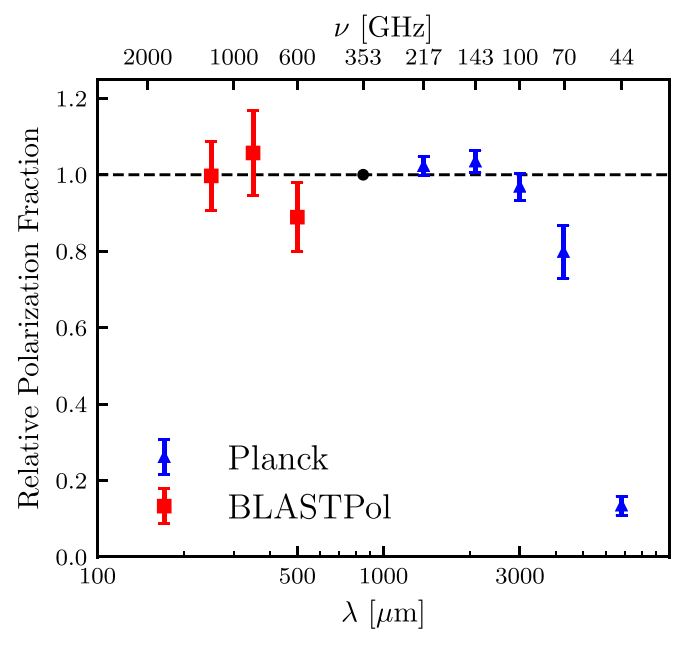


**Figure 13.** The polarization fraction of the dust emission relative to the 850  $\mu$ m (353 GHz) polarization fraction as determined by BLASTPol and Planck observations. The BLASTPol data are from observations in the Vela Molecular Ridge (Ashton et al. 2018) while the Planck data are based on the total and polarized dust SEDs (Planck Collaboration Int. XVII 2014; Planck Collaboration Int. XXII 2015; Planck Collaboration XI 2020) compiled in Table 3. Little wavelength dependence is observed except at the longest wavelengths where AME becomes a significant fraction of the total dust emission.

and 5 over a range of column densities ( $N_{\rm H} \lesssim 5 \times 10^{21}$  cm<sup>-2</sup>, Planck Collaboration Int. XXI 2015; Planck Collaboration XII 2020). We adopt the best-fit value of 4.31 over diffuse sight lines (Planck Collaboration XII 2020) as representative of dust in the diffuse ISM.

These relations between the polarized extinction and polarized emission from interstellar dust allow us to normalize the polarized dust SED derived by Planck Collaboration XI (2020; see Figure 12) to the hydrogen column. First,  $p_{353}/(p_V/\tau_V) = 4.31$ ,  $[p_V/E(B-V)]_{\text{max}} = 0.13$ , and  $R_V = 3.1$  together imply a maximum 353 GHz polarization fraction of 19.6%, agreeing well with the observed maximum of  $p_{353} = 22^{+3.5}_{-1.4}\%$  (Planck Collaboration XII 2020). Applying this polarization fraction to the adopted 353 GHz dust emission per H (see Table 3) yields a maximum 353 GHz polarized dust emission per H of 2.51 ×  $10^{-28} \,\mathrm{erg} \,\mathrm{s}^{-1} \,\mathrm{sr}^{-1} \,\mathrm{H}^{-1}$ . The polarized dust SED of Planck Collaboration XI (2020), which is normalized to unity at 353 GHz, can then be used to compute the maximum polarized dust emission per H at lower frequencies, as presented in Table 3. We have color-corrected all values, including corrections both at the observed frequency and at 353 GHz, to obtain monochromatic spectral energy densities which can be compared directly to models.

Planck Collaboration Int. XXI (2015) also introduced the ratio of the 353 GHz polarized intensity to the *V*-band extinction, i.e.,  $P_{353}/p_V$ . They found a characteristic value of 5.4  $\pm$  0.5 MJy sr<sup>-1</sup> on translucent sight lines integrated over the Planck 353 GHz band. Planck Collaboration XII (2020) extended this analysis to diffuse lines of sight, finding a characteristic ratio of 5.42  $\pm$  0.05 MJy sr<sup>-1</sup> with a systematic decrease to roughly 5 MJy sr<sup>-1</sup> at the lowest ( $\lesssim$ 1  $\times$  10<sup>20</sup> cm<sup>-2</sup>) column densities observed. This ratio is not independent of

values we have already adopted:

$$\frac{P_{353}}{p_V} = \frac{1.086}{R_V} \frac{N_{\rm H}}{E(B-V)} \frac{I_{353}}{N_{\rm H}} \frac{p_{353}}{p_V/\tau_V} = 4.82 \text{ MJy sr}^{-1}, (11)$$

where here  $I_{353}$  and  $P_{353}$  are monochromatic. To compare with the Planck Collaboration XII (2020) value for the 353 GHz band, we must multiply by the color correction factor 1.11 (Planck Collaboration Int. XVII 2014), yielding 5.33 MJy sr<sup>-1</sup> and good agreement. We note, however, that the highly polarized region studied by Panopoulou et al. (2019) has  $P_{353}/p_V = 4.1 \pm 0.1$  MJy sr<sup>-1</sup>, significantly lower than these values. Further study of this ratio and its variability across the sky is needed to understand this apparent discrepancy.

Performing a similar comparison between optical and submillimeter polarization in the Vela C molecular cloud, Santos et al. (2017) related the 600 GHz (500  $\mu$ m) polarization fraction  $p_{600}$ , I band polarized extinction  $p_I$ , and V band total extinction, finding a characteristic  $p_{600}/(p_I/\tau_V)=2.4\pm0.8$ . For a typical Serkowski law (see Section 4.1),  $p_V$  and  $p_I$  differ by only about 10%. If the FIR polarization fraction is relatively flat between 353 and 600 GHz (see Figure 13), then  $p_{600}/(p_I/\tau_V)$  should be approximately 10% larger than  $p_{353}/(p_V/\tau_V)$ , which has characteristic value 4.31 (Planck Collaboration XII 2020). This apparent discrepancy may be due to the very different environments sampled by these observations, but given the importance of this ratio in constraining models, further investigation is warranted.

### 6.3. AME Polarization

If the AME arises from aligned, aspherical grains, then it, too, will be polarized. However, searches for polarized AME have thus far yielded only upper limits at the  $\sim \!\! 1\%$  level (Dickinson et al. 2011; Macellari et al. 2011; Génova-Santos et al. 2015, 2017; Planck Collaboration XXV 2016). See Dickinson et al. (2018) for a recent review.

To the extent that the smallest interstellar grains produce AME through rotational electric dipole radiation, the amount of AME polarization depends on how well these grains are able to align with the local magnetic field. The lack of polarization in the UV extinction curve (see Section 4) despite strong total extinction in the UV (see Section 3.3) suggests that these grains are poorly aligned. However, Hoang et al. (2013) demonstrated that if aligned PAHs were responsible for the claimed detections of polarization in the 2175 Å feature and also produced the AME, then the AME should be polarized at the \$\leq 1\% level, near current upper limits. On the other hand, Draine & Hensley (2016) argued that quantization of the vibrational energy levels in ultrasmall grains leads to exponential suppression of their alignment, resulting in negligible AME polarization.

## 7. Summary and Discussion

Based on the foregoing discussion, we argue that the following data represent the current state of observations that constrain models of interstellar dust, and so a successful model of interstellar dust in the diffuse ISM should be measured against its consistency with these data. We also present a table of constants (Table 5) based on observational data that enables the translation of these observables into constraints on the material properties of dust.

Table 5
Adopted Values of Select Quantities for the Diffuse ISM

	Reference Quantities	
Quantity	Value	References
A(5500 Å)/E(4400 Å–5500 Å)	3.02	Fitzpatrick et al. (2019)
$A_H/A_{K_S}$	1.55	Indebetouw et al. (2005)
$N_{\rm H}/E(B-V)$	$8.8 \times 10^{21}  \mathrm{cm}^{-2}  \mathrm{mag}^{-1}$	Lenz et al. (2017)
$[p_V/E(B-V)]_{\text{max}}$	$0.13 \; {\rm mag^{-1}}$	Planck Collaboration XII (2020)
$p_{353}/(p_V/ au_V)$	4.31	Planck Collaboration XII (2020)
	Derived Quantities	
Quantity	Value	Reference
$R_V$	3.1	Fitzpatrick et al. (2019)
$A_V/N_{ m H}$	$3.5 \times 10^{-22} \text{ mag cm}^2$	•
$p_{353}^{\rm max}$	19.6%	
$P_{353}/p_V$	$4.82 \text{ MJy sr}^{-1}$	

**Note.**  $P_{353}$  in the quantity  $P_{353}/p_V$  is the monochromatic polarized intensity at 353 GHz.

- 1. Abundances: Our adopted ISM abundances, given in Table 2, are based on solar reference abundances (Asplund et al. 2009; Scott et al. 2015a, 2015b) corrected for diffusion (Turcotte & Wimmer-Schweingruber 2002) and with chemical enrichment (Chiappini et al. 2003; Bedell et al. 2018). Solid-phase abundances are then derived based on the gas-phase abundances determined by Jenkins (2009) for sight lines with moderate depletion  $(F_* = 0.5)$ .
- 2. Extinction: We synthesize the extinction curves of Gordon et al. (2009) and Cardelli et al. (1989) in the FUV, which we join to that of Fitzpatrick et al. (2019) in the UV through the optical. From 0.55 to 2.2  $\mu$ m, we employ the extinction curve of Schlafly et al. (2016) assuming  $A_H/A_K=1.55$  (Indebetouw et al. 2005). From 2.2 to 37  $\mu$ m, we adopt the MIR extinction curve derived by Hensley & Draine (2020) on the sight line toward Cyg OB2-12. Finally, we normalize this composite curve to the hydrogen column via  $N_H/E(B-V)=8.8\times10^{21}\,\mathrm{cm}^{-2}\,\mathrm{mag}^{-1}$  (Lenz et al. 2017).
- 3. Polarized Extinction: Between 0.12 and 4  $\mu$ m, we join a Serkowski law with parameters K=0.87 and  $\lambda_{\rm max}=0.55~\mu$ m (Whittet 2003) smoothly to a power law with index  $\beta=1.6$  in the IR (Martin et al. 1992). We normalize this curve to a maximum starlight polarization of  $p_V/E(B-V)=0.13~{\rm mag}^{-1}$  (Panopoulou et al. 2019; Planck Collaboration XII 2020).
- 4. *Emission*: In the MIR, we adopt the AKARI and Spitzer spectrum of a sample of PAH-bright galaxies (Lai et al. 2020) between 3 and 12  $\mu$ m and the Spitzer IRS observations of the translucent cloud DCld 300.2–16.9 (B) (Ingalls et al. 2011) between 6 and 38  $\mu$ m. The composite spectrum is scaled to the hydrogen column to match observations of diffuse Galactic emission in the DIRBE bands (Dwek et al. 1997). In the FIR, we adopt the H I-correlated dust emission measured in the DIRBE and Planck bands with  $\nu \geqslant 353$  GHz (Planck Collaboration Int. XVII 2014), and the 353 GHz-correlated emission measured in the lower frequency Planck and WMAP bands by Planck Collaboration Int. XXII (2015).

5. *Polarized Emission*: We adopt the frequency dependence of the polarized infrared emission determined by Planck Collaboration XI (2020) scaled to match the relation between polarized extinction and emission derived by Planck Collaboration XII (2020).

These constraints are summarized visually in Figure 14, which illustrates the impressive breadth of our current knowledge, spanning a large dynamic range in wavelength, magnitudes of extinction, and intensity. It also highlights the most pressing needs for augmenting the state of art. We close by highlighting a few such future directions of key importance for dust modeling.

The spectroscopic features in extinction, emission, and polarization are the "fingerprints" of the specific materials that constitute interstellar grains, enabling the determination of their chemical makeup. The Near InfraRed spectrograph (NIRSpec,  $0.6-5 \mu m$ ; Bagnasco et al. 2007) and Mid-Infrared Instrument (MIRI, 5–28  $\mu$ m; Rieke et al. 2015) aboard the James Webb Space Telescope (JWST) will characterize the NIR and MIR spectroscopic dust features in unprecedented detail. Observing the full sky between 0.75 and 5  $\mu$ m with a resolving power of up to 130, SPHEREx (Doré et al. 2016) will enable mapping of the strength of dust absorption and emission features and thus probe their variation with location in the Galaxy. The high spectral resolution of the XRISM (XRISM Science Team 2020) and Athena (Barcons et al. 2017) X-ray observatories promises to reveal the mineralogical composition of interstellar grains in ways complementary to what can be gleaned from the infrared features.

As the 3.4  $\mu$ m complex has been observed on very few sight lines that might typify the diffuse ISM, a number of questions can be addressed by more sensitive observations. Is it indeed generic of the diffuse ISM that the 3.3  $\mu$ m aromatic feature is substantially broader in absorption than emission? To what extent does diamond-like carbon contribute emission and absorption in the 3.47  $\mu$ m feature? How does the 3.4  $\mu$ m profile change systematically with interstellar environment?

The 6.2 and 7.7  $\mu$ m aromatic features have been observed in absorption, but on few sight lines. Detailed characterization of

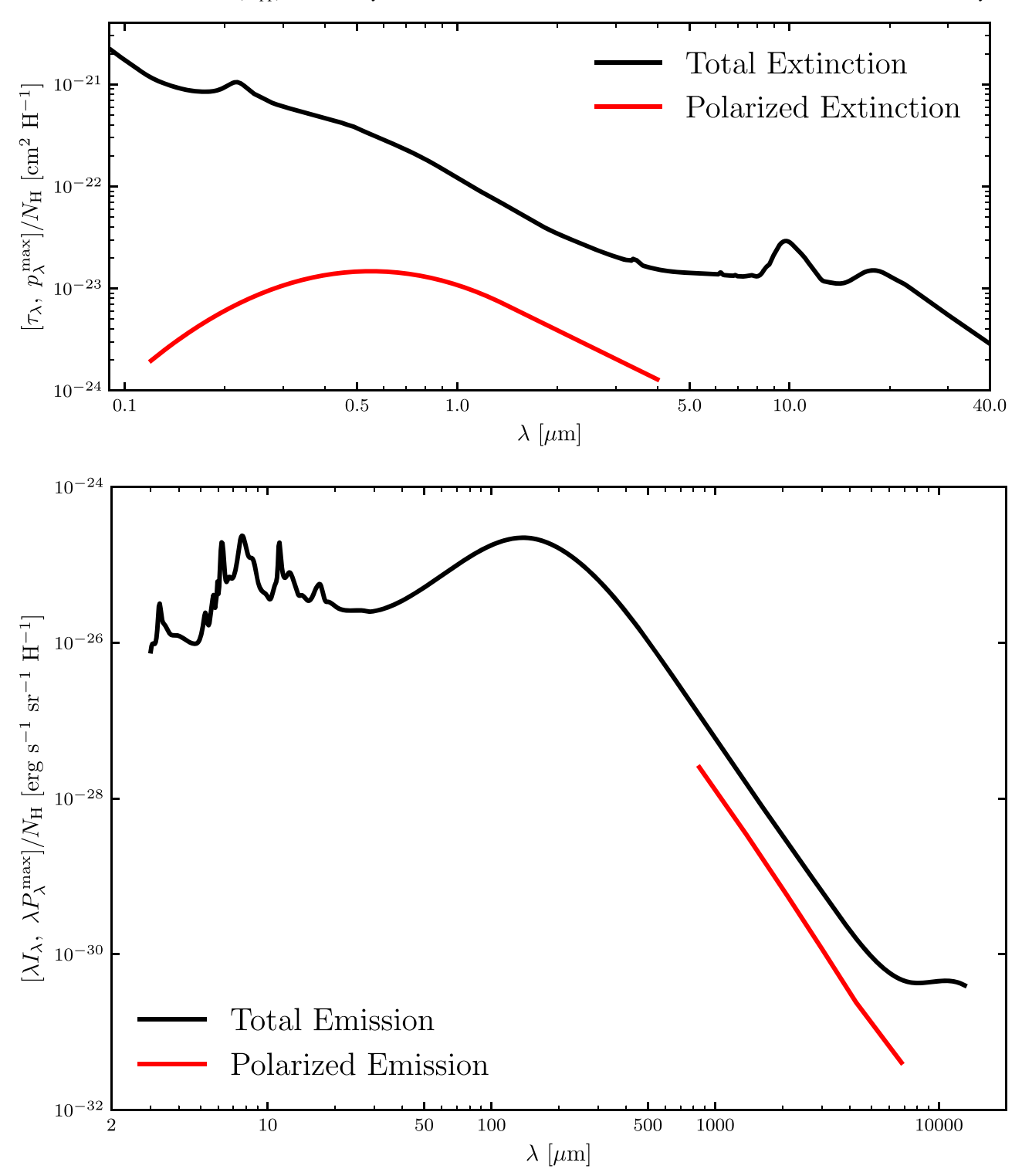


**Figure 14.** In the top panel, we plot our adopted constraints on the total (black) and polarized (red) extinction from dust in the diffuse ISM. In the bottom panel, we plot our adopted constraints on the total (black) and polarized (red) emission from interstellar dust. Note that for both polarized extinction and emission, we show the maximum level of polarization, corresponding to the interstellar magnetic field lying in the plane of the sky. We have made use of the values in Table 5 where necessary to normalize the observational data to the hydrogen column. The data underlying the FIR emission constraints, including uncertainties, are presented in Table 3. A summary of the adopted constraints is given in Section 7. The extrapolation of the extinction curve to FIR wavelengths can be found in Hensley & Draine (2020).

(The data used to create this figure are available.)

these features, particularly comparison of the emission and absorption profiles, will clarify which grains are the carriers of aromatic material in the ISM. The aromatic features at still longer wavelengths have not been observed in absorption, making them a compelling target for JWST and an important constraint on PAH models.

While the aliphatic 6.85  $\mu m$  feature appears generic to the diffuse ISM on the basis of its detection in absorption toward Cyg OB2-12, the ubiquity of the 7.25  $\mu m$  methylene feature is less clear. Characterization of these aliphatic absorption features and their strengths relative to the aromatic features is a relatively unexplored window into the hydrocarbon chemistry of the ISM which JWST will enable. Likewise, the deuterated counterparts of both the aliphatic and aromatic features, inaccessible from the ground, will be accessible to JWST and SPHEREx in emission and absorption.

The sensitivity of MIRI will enable searches for as-yet undetected spectroscopic features and will characterize in greater detail those already observed. The silicate features can be probed for trace amounts of crystallinity, and the detection of crystalline forsterite can be verified on many more sight lines. Dedicated searches can be undertaken for the  $11.2 \, \mu m$  SiC feature and the  $11.53 \, \mu m$  feature from polycrystalline graphite, perhaps finally confirming or ruling out graphite as a major constituent of interstellar dust.

In the NIR, NIRSpec can characterize the many DIBs found longward of 600 nm and perform sensitive searches for new ones. Likewise, the presence or absence of predicted features at 1.05 and 1.26  $\mu$ m from ionized PAHs can be strongly constrained.

While we anticipate advances in infrared spectroscopy, it is unfortunate that this is not the case for infrared spectropolarimetry. Polarimetry is a powerful complementary constraint on the properties of interstellar dust, particularly given the dichotomy observed in polarization between carbonaceous and silicate features. Additionally, the profiles of the spectroscopic features in extinction and polarization generically differ because each depends differently on the optical constants, and so measurement of both strongly constrains grain material properties. Additional spectropolarimetric measurements of the 9.7 and 18  $\mu$ m silicate features and the 3.4  $\mu$ m carbonaceous feature are desperately needed. In addition, the continuum polarization between 4 and  $8 \mu m$  is poorly determined. Unfortunately, we are unaware of any operational facilities, nor of any planned ones, capable of spectropolarimetry or even broadband polarimetry between 3 and 8  $\mu$ m. However, new polarimetric measurements of the 9.7  $\mu$ m silicate feature are possible with CanariCam (Packham et al. 2005).

Stellar optical polarimetry, on the other hand, will be pushed to high-latitude, diffuse sight lines in the 2020s with the PASIPHAE survey (Tassis et al. 2018). With a many-fold expansion of stellar polarization catalogs, new insights will be gained in the variations in the polarized extinction curve throughout the Galaxy, including its connection to polarized infrared emission.

Because of the role of dust polarization in mapping magnetic fields and as a contaminant for cosmic microwave background (CMB) polarization science, the prospects are better for studies of polarized emission. Of critical importance from the perspective of dust modeling is extending coverage of the polarized dust SED to higher frequencies on sight lines that might typify the diffuse ISM. Measuring the wavelength dependence of polarization near the peak of the dust SED will allow the contributions from different dust populations to be more efficiently disentangled. At even shorter wavelengths, we expect emission to be dominated by smaller, unaligned grains. While such measurements are already possible on dense sight lines using instruments like HAWC+ aboard SOFIA

(Harper et al. 2018), the greater sensitivity afforded by upcoming facilities like CCAT-prime ( $260 \leqslant \nu/\text{GHz} \leqslant 860$ ; Stacey et al. 2018) is required to access diffuse sight lines. However, we are unaware of upcoming facilities that can perform polarimetry on the Wien side of the dust SED along diffuse sight lines.

Particularly given the uncertainties in the level of polarization in the AME and the abundance of material able to emit microwave magnetic dipole radiation, extension of the determination of the polarized dust SED to lower frequencies is also of great interest. Such measurements will be made by upcoming CMB experiments such as the Simons Observatory (Ade et al. 2019), LiteBIRD (Matsumura et al. 2014), and CMB-S4 (Abazajian et al. 2019), all of which have the sensitivity to characterize dust emission on the diffuse, highlatitude sight lines of greatest interest to this work.

These directions are but a few avenues to be explored with the wealth of upcoming data and are not intended to be exhaustive. As we emphasize in this work, dust modeling should be informed by the full range of optical phenomena associated with interstellar dust. By combining the insights gleaned from a variety of observations across the electromagnetic spectrum, we can paint the clearest picture possible of the nature of interstellar grains.

We are grateful to many stimulating conversations that informed this work over its long completion. We thank in particular Megan Bedell, Simone Bianchi, Tuhin Ghosh, Vincent Guillet, Ed Jenkins, Eddie Schlafly, Adolf Witt, and Chris Wright for sharing their expertise. We thank Jim Ingalls for providing the Spitzer IRS spectrum of DCld 300.2-16.9, and Thomas Lai and JD Smith for providing their "1C" PAH spectrum in advance of publication. We thank the anonymous referee for helpful comments. This research was carried out in part at the Jet Propulsion Laboratory, California Institute of Technology, under a contract with the National Aeronautics and Space Administration. This work was supported in part by NSF grants AST-1408723 and AST-1908123. B.H. acknowledges support from the National Science Foundation Graduate Research Fellowship under grant No. DGE-0646086 during the earliest stages of this work.

*Software:* Astropy (Astropy Collaboration et al. 2013, 2018), Matplotlib (Hunter 2007), NumPy (van der Walt et al. 2011), SciPy (Virtanen et al. 2020).

### **ORCID iDs**

Brandon S. Hensley https://orcid.org/0000-0001-7449-4638 B. T. Draine https://orcid.org/0000-0002-0846-936X

#### References

Abazajian, K., Addison, G., Adshead, P., et al. 2019, arXiv:1907.04473
Adamson, A. J., Whittet, D. C. B., Chrysostomou, A., et al. 1999, ApJ, 512, 224
Adamson, A. J., Whittet, D. C. B., & Duley, W. W. 1990, MNRAS, 243, 400
Ade, P., Aguirre, J., Ahmed, Z., et al. 2019, JCAP, 2019, 056
Aitken, D. K., Bailey, J. A., Roche, P. F., & Hough, J. M. 1985, MNRAS, 215, 815
Aitken, D. K., Smith, C. H., & Roche, P. F. 1989, MNRAS, 236, 919
Allamandola, L. J., Sandford, S. A., Tielens, A. G. G. M., & Herbst, T. M. 1992, ApJ, 399, 134
Allamandola, L. J., Tielens, A. G. G. M., & Barker, J. R. 1985, ApJL, 290, L25
Allamandola, L. J., Tielens, A. G. G. M., & Barker, J. R. 1985, ApJL, 290, L25
Allamandola, L. J., Tielens, A. G. G. M., & Barker, J. R. 1985, ApJS, 71, 733
Andersson, B.-G., Lazarian, A., & Vaillancourt, J. E. 2015, ARA&A, 53, 501
Ashton, P. C., Ade, P. A. R., Angilè, F. E., et al. 2018, ApJ, 857, 10

```
Asplund, M., Grevesse, N., Sauval, A. J., & Scott, P. 2009, ARA&A, 47, 481
Astropy Collaboration, Price-Whelan, A. M., Sipőcz, B. M., et al. 2018, AJ,
   156, 123
Astropy Collaboration, Robitaille, T. P., Tollerud, E. J., et al. 2013, A&A,
  558, A33
Bagnasco, G., Kolm, M., Ferruit, P., et al. 2007, Proc. SPIE, 6692, 66920M
Barcons, X., Barret, D., Decourchelle, A., et al. 2017, AN, 338, 153
Barker, J. R., Allamandola, L. J., & Tielens, A. G. G. M. 1987, ApJL, 315, L61
Bedell, M., Bean, J. L., Meléndez, J., et al. 2018, ApJ, 865, 68
Behr, A. 1959, ZAp, 47, 54
Bennett, C. L., Larson, D., Weiland, J. L., et al. 2013, ApJS, 208, 20
Benoît, A., Ade, P., Amblard, A., et al. 2004, A&A, 424, 571
Benoît, A. 2002, in AIP Conf. Ser. 616, Experimental Cosmology at Millimetre
   Wavelengths, ed. M. de Petris & M. Gervasi (Melville, NY: AIP), 31
Bensby, T., & Feltzing, S. 2006, MNRAS, 367, 1181
Bensby, T., Feltzing, S., Lundström, I., & Ilyin, I. 2005, A&A, 433, 185
Berné, O., Cox, N. L. J., Mulas, G., & Joblin, C. 2017, A&A, 605, L1
Bertoldi, F., Timmermann, R., Rosenthal, D., Drapatz, S., & Wright, C. M.
   1999, A&A, 346, 267
Bianchi, S., Giovanardi, C., Smith, M. W. L., et al. 2017, A&A, 597, A130
Blanco, V. M. 1957, ApJ, 125, 209
Bless, R. C., & Savage, B. D. 1972, ApJ, 171, 293
Bohlin, R. C., Savage, B. D., & Drake, J. F. 1978, ApJ, 224, 132
Bowey, J. E., Adamson, A. J., & Whittet, D. C. B. 1998, MNRAS, 298, 131
Brandt, T. D., & Draine, B. T. 2012, ApJ, 744, 129
Brooke, T. Y., Sellgren, K., & Smith, R. G. 1996, ApJ, 459, 209
Brown, M. J. I., Moustakas, J., Smith, J.-D. T., et al. 2014, ApJS, 212, 18
Butchart, I., McFadzean, A. D., Whittet, D. C. B., Geballe, T. R., &
   Greenberg, J. M. 1986, A&A, 154, L5
Campbell, E. K., Holz, M., Gerlich, D., & Maier, J. P. 2015, Natur, 523, 322
Cardelli, J. A., Clayton, G. C., & Mathis, J. S. 1988, ApJL, 329, L33
Cardelli, J. A., Clayton, G. C., & Mathis, J. S. 1989, ApJ, 345, 245 Catura, R. C. 1983, ApJ, 275, 645
Chapman, N. L., Mundy, L. G., Lai, S.-P., & Evans, N. J., II 2009, ApJ,
   690, 496
Chen, X., Wang, S., Deng, L., & de Grijs, R. 2018, ApJ, 859, 137
Chiappini, C., Romano, D., & Matteucci, F. 2003, MNRAS, 339, 63
Chiar, J. E., Adamson, A. J., Whittet, D. C. B., et al. 2006, ApJ, 651, 268
Chiar, J. E., & Tielens, A. G. G. M. 2006, ApJ, 637, 774
Chiar, J. E., Tielens, A. G. G. M., Adamson, A. J., & Ricca, A. 2013, ApJ,
Chiar, J. E., Tielens, A. G. G. M., Whittet, D. C. B., et al. 2000, ApJ, 537, 749
Choi, S. K., & Page, L. A. 2015, JCAP, 12, 020
Clayton, G. C., Anderson, C. M., Magalhaes, A. M., et al. 1992, ApJL,
   385, L53
Clayton, G. C., Gordon, K. D., Salama, F., et al. 2003, ApJ, 592, 947
Clayton, G. C., & Martin, P. G. 1985, ApJ, 288, 558
Clayton, G. C., & Mathis, J. S. 1988, ApJ, 327, 911
Cohen, M., Anderson, C. M., Cowley, A., et al. 1975, ApJ, 196, 179
Compiègne, M., Verstraete, L., Jones, A., et al. 2011, A&A, 525, A103
Cordiner, M. A., Linnartz, H., Cox, N. L. J., et al. 2019, ApJL, 875, L28
Costantini, E., Freyberg, M. J., & Predehl, P. 2005, A&A, 444, 187
Costantini, E., Pinto, C., Kaastra, J. S., et al. 2012, A&A, 539, A32
Coyne, G. V., Gehrels, T., & Serkowski, K. 1974, AJ, 79, 581
Darbon, S., Perrin, J. M., & Sivan, J. P. 1999, A&A, 348, 990
Davis, L., Jr., & Greenstein, J. L. 1951, ApJ, 114, 206
de Oliveira-Costa, A., Kogut, A., Devlin, M. J., et al. 1997, ApJL, 482, L17
Demyk, K., Jones, A. P., Dartois, E., Cox, P., & D'Hendecourt, L. 1999, A&A,
   349, 267
Dickinson, C., Ali-Haïmoud, Y., Barr, A., et al. 2018, NewAR, 80, 1
Dickinson, C., Barr, A., Chiang, H. C., et al. 2019, MNRAS, 485, 2844
Dickinson, C., Peel, M., & Vidal, M. 2011, MNRAS, 418, L35
Diplas, A., & Savage, B. D. 1994, ApJ, 427, 274
Do-Duy, T., Wright, C. M., Fujiyoshi, T., et al. 2020, MNRAS, 493, 4463
Doney, K. D., Candian, A., Mori, T., Onaka, T., & Tielens, A. G. G. M. 2016,
     &A, 586, A65
Donn, B. 1968, AJS, 73, 10
Doré, O., Werner, M. W., Ashby, M., et al. 2016, arXiv:1606.07039
Draine, B. 1989a, in IAU Symp. 135, Interstellar Dust, ed. L. J. Allamandola &
   A. G. G. M. Tielens (Dordrecht: Kluwer), 313
Draine, B. T. 1984, ApJL, 277, L71
Draine, B. T. 1989b, in ESA Special Publication, Vol. 290, Infrared
   Spectroscopy in Astronomy, ed. B. H. Kaldeich (Paris: ESA), 93
Draine, B. T. 2003a, ARA&A, 41, 241
Draine, B. T. 2003b, ApJ, 598, 1026
Draine, B. T. 2016, ApJ, 831, 109
```

```
Draine, B. T., & Allaf-Akbari, K. 2006, ApJ, 652, 1318
Draine, B. T., & Fraisse, A. A. 2009, ApJ, 696, 1
Draine, B. T., & Hensley, B. S. 2016, ApJ, 831, 59
Draine, B. T., & Lazarian, A. 1998, ApJL, 494, L19
Draine, B. T., & Lee, H. M. 1984, ApJ, 285, 89
Draine, B. T., & Li, A. 2007, ApJ, 657, 810
Draine, B. T., & Malhotra, S. 1993, ApJ, 414, 632
Duley, W. W., & Hu, A. 2012, ApJ, 761, 115
Duley, W. W., & Williams, D. A. 1983, MNRAS, 205, 67P
Dwek, E., Arendt, R. G., Fixsen, D. J., et al. 1997, ApJ, 475, 565
Dyck, H. M., & Beichman, C. A. 1974, ApJ, 194, 57
Dyck, H. M., Capps, R. W., & Beichman, C. A. 1974, ApJL, 188, L103
Dyck, H. M., Capps, R. W., Forrest, W. J., & Gillett, F. C. 1973, ApJL,
Dyck, H. M., & Lonsdale, C. J. 1981, in IAU Symp. 96, Infrared Astronomy,
  ed. C. G. Wynn-Williams & D. P. Cruikshank (Dordrecht: Reidel), 223
Elvey, C. T., & Roach, F. E. 1937, ApJ, 85, 213
Fan, H., Hobbs, L. M., Dahlstrom, J. A., et al. 2019, ApJ, 878, 151
Fanciullo, L., Guillet, V., Aniano, G., et al. 2015, A&A, 580, A136
Fitzpatrick, E. L. 1985, ApJ, 299, 219
Fitzpatrick, E. L. 1986, AJ, 92, 1068
Fitzpatrick, E. L., & Massa, D. 1986, ApJ, 307, 286
Fitzpatrick, E. L., & Massa, D. 1988, ApJ, 328, 734
Fitzpatrick, E. L., & Massa, D. 2005, AJ, 130, 1127
Fitzpatrick, E. L., & Massa, D. 2009, ApJ, 699, 1209
Fitzpatrick, E. L., Massa, D., Gordon, K. D., Bohlin, R., & Clayton, G. C.
  2019, ApJ, 886, 108
Flaherty, K. M., Pipher, J. L., Megeath, S. T., et al. 2007, ApJ, 663, 1069
Fogerty, S., Forrest, W., Watson, D. M., Sargent, B. A., & Koch, I. 2016, ApJ,
  830.71
Forrest, W. J., Gillett, F. C., & Stein, W. A. 1975, ApJ, 195, 423
Forrest, W. J., McCarthy, J. F., & Houck, J. R. 1979, ApJ, 233, 611
Fritz, T. K., Gillessen, S., Dodds-Eden, K., et al. 2011, ApJ, 737, 73
Furton, D. G., & Witt, A. N. 1990, ApJL, 364, L45
Furton, D. G., & Witt, A. N. 1992, ApJ, 386, 587
Gandilo, N. N., Ade, P. A. R., Angilè, F. E., et al. 2016, ApJ, 824, 84
Gao, J., Jiang, B. W., & Li, A. 2009, ApJ, 707, 89
Geballe, T. R., Lacy, J. H., Persson, S. E., McGregor, P. J., & Soifer, B. T.
  1985, ApJ, 292, 500
Gehrels, T. 1960, AJ, 65, 470
Gehrels, T. 1974, AJ, 79, 590
Génova-Santos, R., Martín, J. A. R., Rebolo, R., et al. 2015, MNRAS,
  452, 4169
Génova-Santos, R., Rubiño-Martín, J. A., Peláez-Santos, A., et al. 2017,
   MNRAS, 464, 4107
Gillett, F. C., Forrest, W. J., & Merrill, K. M. 1973, ApJ, 183, 87
Gillett, F. C., Low, F. J., & Stein, W. A. 1968, ApJ, 154, 677
Gordon, K. D., Cartledge, S., & Clayton, G. C. 2009, ApJ, 705, 1320
Gordon, K. D., Cartledge, S., & Clayton, G. C. 2014, ApJ, 781, 128
Gordon, K. D., Clayton, G. C., Misselt, K. A., Landolt, A. U., & Wolff, M. J.
  2003, ApJ, 594, 279
Gordon, K. D., Witt, A. N., & Friedmann, B. C. 1998, ApJ, 498, 522
Green, G. M., Schlafly, E. F., Finkbeiner, D., et al. 2018, MNRAS, 478, 651
Guhathakurta, P., & Tyson, J. A. 1989, ApJ, 346, 773
Guillet, V., Fanciullo, L., Verstraete, L., et al. 2018, A&A, 610, A16
Hall, J. S. 1949, Sci, 109, 166
Hall, J. S., & Mikesell, A. H. 1949, AJ, 54, 187
Hall, J. S., & Mikesell, A. H. 1950, PUSNO, 17, 3
Harper, D. A., Runyan, M. C., Dowell, C. D., et al. 2018, JAI, 7, 1840008
Hayakawa, S. 1970, PThPh, 43, 1224
Heger, M. L. 1922a, LicOB, 10, 141
Heger, M. L. 1922b, LicOB, 10, 146
Heiles, C. 1976, ApJ, 204, 379
Heng, K., & Draine, B. T. 2009, arXiv:0906.0773
Hennebelle, P., Pérault, M., Teyssier, D., & Ganesh, S. 2001, A&A, 365, 598
Hensley, B. S., & Draine, B. T. 2020, ApJ, 895, 38
Hensley, B. S., Draine, B. T., & Meisner, A. M. 2016, ApJ, 827, 45
Henyey, L. G., & Greenstein, J. L. 1941, ApJ, 93, 70
Herbig, G. H. 1995, ARA&A, 33, 19
HI4PI Collaboration, ben Bekhti, N., Flöer, L., et al. 2016, A&A, 594, A116
Hiltner, W. A. 1949a, ApJ, 109, 471
Hiltner, W. A. 1949b, Sci, 109, 165
Hiltner, W. A. 1949c, Natur, 163, 283
Hoang, T., & Lazarian, A. 2018, ApJ, 860, 158
Hoang, T., Lazarian, A., & Martin, P. G. 2013, ApJ, 779, 152
Hobbs, L. M., York, D. G., Thorburn, J. A., et al. 2009, ApJ, 705, 32
```

```
Hoffman, J., & Draine, B. T. 2016, ApJ, 817, 139
Hosek, M. W. J., Lu, J. R., Anderson, J., et al. 2018, ApJ, 855, 13
Hough, J. H., Whittet, D. C. B., Sato, S., et al. 1989, MNRAS, 241, 71
Humphreys, R. M. 1978, ApJS, 38, 309
Hunter, J. D. 2007, CSE, 9, 90
Indebetouw, R., Mathis, J. S., Babler, B. L., et al. 2005, ApJ, 619, 931
Ingalls, J. G., Bania, T. M., Boulanger, F., et al. 2011, ApJ, 743, 174
Ishii, M., Nagata, T., Chrysostomou, A., & Hough, J. H. 2002, AJ, 124, 2790
Jenkins, E. B. 2009, ApJ, 700, 1299
Jiang, B. W., Gao, J., Omont, A., Schuller, F., & Simon, G. 2006, A&A,
   446, 551
Jiang, B. W., Omont, A., Ganesh, S., Simon, G., & Schuller, F. 2003, A&A,
   400, 903
Joblin, C., Leger, A., & Martin, P. 1992, ApJL, 393, L79
Joblin, C., Tielens, A. G. G. M., Allamandola, L. J., & Geballe, T. R. 1996,
   ApJ, 458, 610
Johnson, H. L., & Borgman, J. 1963, BAN, 17, 115
Jones, T. J., & Gehrz, R. D. 1990, AJ, 100, 274
Kalberla, P. M. W., Burton, W. B., Hartmann, D., et al. 2005, A&A, 440, 775
Kemper, F., Vriend, W. J., & Tielens, A. G. G. M. 2004, ApJ, 609, 826
Kemper, F., Vriend, W. J., & Tielens, A. G. G. M. 2005, ApJ, 633, 534
Knapp, G. R., & Kerr, F. J. 1974, A&A, 35, 361
Kogut, A., Banday, A. J., Bennett, C. L., et al. 1996, ApJ, 460, 1
Koornneef, J. 1983, A&A, 128, 84
Krachmalnicoff, N., Carretti, E., Baccigalupi, C., et al. 2018, A&A, 618, A166
Lai, T. S. Y., Smith, J. D. T., Baba, S., Spoon, H. W. W., & Imanishi, M. 2020,
Lai, T. S. Y., Witt, A. N., & Crawford, K. 2017, MNRAS, 469, 4933
Lan, T.-W., Ménard, B., & Zhu, G. 2015, MNRAS, 452, 3629
Lee, J. C., Xiang, J., Ravel, B., Kortright, J., & Flanagan, K. 2009, ApJ,
   702, 970
Leger, A., D'Hendecourt, L., & Boissel, P. 1988, PhRvL, 60, 921
Leger, A., & Puget, J. L. 1984, A&A, 137, L5
Leitch, E. M., Readhead, A. C. S., Pearson, T. J., & Myers, S. T. 1997, ApJL,
   486, L23
Lenz, D., Hensley, B. S., & Doré, O. 2017, ApJ, 846, 38
Li, A., & Draine, B. T. 2012, ApJL, 760, L35
Li, Q., Liang, S. L., & Li, A. 2014, MNRAS, 440, L56
Lillie, C. F., & Witt, A. N. 1976, ApJ, 208, 64
Linsky, J. L., Draine, B. T., Moos, H. W., et al. 2006, ApJ, 647, 1106
Liszt, H. 2014, ApJ, 780, 10
Lodders, K., Palme, H., & Gail, H.-P. 2009, LanB, 4, 712
Lutz, D. 1999, in ESA Special Publication, Vol. 427, The Universe as Seen by
  ISO, ed. P. Cox & M. Kessler (Paris: ESA), 623
Lutz, D., Feuchtgruber, H., Genzel, R., et al. 1996, A&A, 315, L269
Macellari, N., Pierpaoli, E., Dickinson, C., & Vaillancourt, J. E. 2011,
   MNRAS, 418, 888
Maíz Apellániz, J. 2013, in Proc. X Scientific Meeting of the Spanish
   Astronomical Society (SEA), Highlights of Spanish Astrophysics VII, ed.
   J. C. Guirado, L. M. Lara, V. Quilis et al. (Valencia: Spanish Astronomical
   Society), 583
Maíz Apellániz, J., Evans, C. J., Barbá, R. H., et al. 2014, A&A, 564, A63
Maíz Apellániz, J., Pantaleoni González, M., Barbá, R. H., García-Lario, P., &
   Nogueras-Lara, F. 2020, MNRAS, 496, 4951
Marchenko, S. V., & Moffat, A. F. J. 2017, MNRAS, 468, 2416
Martin, P. G. 1970, MNRAS, 149, 221
Martin, P. G., Adamson, A. J., Whittet, D. C. B., et al. 1992, ApJ, 392, 691
Martin, P. G., Clayton, G. C., & Wolff, M. J. 1999, ApJ, 510, 905
Martin, P. G., & Whittet, D. C. B. 1990, ApJ, 357, 113
Mason, R. E., Wright, G. S., Adamson, A., & Pendleton, Y. 2007, ApJ,
   656, 798
Massa, D., Fitzpatrick, E. L., & Gordon, K. D. 2020, ApJ, 891, 67
Mathis, J. S. 1990, ARA&A, 28, 37
Mathis, J. S., Rumpl, W., & Nordsieck, K. H. 1977, ApJ, 217, 425
Matsumura, T., Akiba, Y., Borrill, J., et al. 2014, JLTP, 176, 733
Mattioda, A. L., Allamandola, L. J., & Hudgins, D. M. 2005a, ApJ, 629,
Mattioda, A. L., Hudgins, D. M., & Allamandola, L. J. 2005b, ApJ, 629, 1188
Mauche, C. W., & Gorenstein, P. 1986, ApJ, 302, 371
McCarthy, J. F., Forrest, W. J., Briotta, D. A., Jr., & Houck, J. R. 1980, ApJ,
  242, 965
Mennella, V., Colangeli, L., Bussoletti, E., Palumbo, P., & Rotundi, A. 1998,
   ApJL, 507, L177
Merrill, K. M., Soifer, B. T., & Russell, R. W. 1975, ApJL, 200, L37
Merrill, P. W. 1936, ApJ, 83, 126
```

Mirabel, I. F., & Gergely, T. E. 1979, A&A, 77, 110

```
Misselt, K. A., Clayton, G. C., & Gordon, K. D. 1999, ApJ, 515, 128
Miville-Deschênes, M.-A., Ysard, N., Lavabre, A., et al. 2008, A&A,
  490, 1093
Morgan, W. W., Harris, D. L., & Johnson, H. L. 1953, ApJ, 118, 92
Murthy, J., Henry, R. C., & Holberg, J. B. 1994, ApJ, 428, 233
Nagata, T. 1990, ApJL, 348, L13
Nagata, T., Kobayashi, N., & Sato, S. 1994, ApJL, 423, L113
Nagatomo, S., Nagata, T., & Nishiyama, S. 2019, PASJ, 71, 106
Nataf, D. M., Gould, A., Fouqué, P., et al. 2013, ApJ, 769, 88
Nguyen, H., Dawson, J. R., Miville-Deschênes, M.-A., et al. 2018, ApJ,
Nieva, M.-F., & Przybilla, N. 2012, A&A, 539, A143
Nishiyama, S., Nagata, T., Kusakabe, N., et al. 2006, ApJ, 638, 839
Nishiyama, S., Nagata, T., Tamura, M., et al. 2008, ApJ, 680, 1174
Nishiyama, S., Tamura, M., Hatano, H., et al. 2009, ApJ, 696, 1407
Nogueras-Lara, F., Schödel, R., Neumayer, N., et al. 2020, A&A, 641, A141
Overbeck, J. W. 1965, ApJ, 141, 864
Packham, C., Hough, J. H., & Telesco, C. M. 2005, in ASP Conf. Ser. 343,
   Astronomical Polarimetry: Current Status and Future Directions, ed.
   A. Adamson et al. (San Francisco, CA: ASP), 38
Paerels, F., Brinkman, A. C., van der Meer, R. L. J., et al. 2001, ApJ,
  546, 338
Panopoulou, G. V., Hensley, B. S., Skalidis, R., Blinov, D., & Tassis, K. 2019,
   A&A, 624, L8
Paradis, D., Bernard, J.-P., Mény, C., & Gromov, V. 2011, A&A, 534, A118
Peek, J. E. G., Heiles, C., Douglas, K. A., et al. 2011, ApJS, 194, 20
Peeters, E., Allamandola, L. J., Bauschlicher, C. W. J., et al. 2004, ApJ,
  604, 252
Pendleton, Y. J., & Allamandola, L. J. 2002, ApJS, 138, 75
Pendleton, Y. J., Sandford, S. A., Allamandola, L. J., Tielens, A. G. G. M., &
  Sellgren, K. 1994, ApJ, 437, 683
Planck Collaboration Int. LVII 2020, A&A, 643, 42
Planck Collaboration Int. XIX 2015, A&A, 576, A104
Planck Collaboration Int. XV 2014, A&A, 565, A103
Planck Collaboration Int. XVII 2014, A&A, 566, A55
Planck Collaboration Int. XXI 2015, A&A, 576, A106
Planck Collaboration Int. XXII 2015, A&A, 576, A107
Planck Collaboration Int. XXIX 2016, A&A, 586, A132
Planck Collaboration X 2016, A&A, 594, A10
Planck Collaboration XI 2014, A&A, 571, A11
Planck Collaboration XI 2020, A&A, 641, A11
Planck Collaboration XII 2020, A&A, 641, A12
Planck Collaboration XXV 2016, A&A, 594, A25
Poteet, C. A., Whittet, D. C. B., & Draine, B. T. 2015, ApJ, 801, 110
Prevot, M. L., Lequeux, J., Prevot, L., Maurice, E., & Rocca-Volmerange, B.
   1984, A&A, 132, 389
Rachford, B. L., Snow, T. P., Destree, J. D., et al. 2009, ApJS, 180, 125
Rieke, G. H. 1974, ApJL, 193, L81
Rieke, G. H., & Lebofsky, M. J. 1985, ApJ, 288, 618
Rieke, G. H., Wright, G. S., Böker, T., et al. 2015, PASP, 127, 584
Rocca-Volmerange, B., Prevot, L., Prevot-Burnichon, M. L., Ferlet, R., &
  Lequeux, J. 1981, A&A, 99, L5
Roche, P. F., & Aitken, D. K. 1985, MNRAS, 215, 425
Rogantini, D., Costantini, E., Zeegers, S. T., et al. 2019, A&A, 630, A143
Rogantini, D., Costantini, E., Zeegers, S. T., et al. 2020, A&A, 641, A149
Román-Zúñiga, C. G., Lada, C. J., Muench, A., & Alves, J. F. 2007, ApJ,
  664, 357
Rosenthal, D., Bertoldi, F., & Drapatz, S. 2000, A&A, 356, 705
Sandford, S. A., Allamandola, L. J., Tielens, A. G. G. M., et al. 1991, ApJ,
  371, 607
Santos, F. P., Ade, P. A. R., Angilè, F. E., et al. 2017, ApJ, 837, 161
Sasseen, T. P., Hurwitz, M., Dixon, W. V., & Airieau, S. 2002, ApJ, 566, 267
Savage, B. D. 1975, ApJ, 199, 92
Schiminovich, D., Friedman, P. G., Martin, C., & Morrissey, P. F. 2001, ApJL,
  563, L161
Schlafly, E. F., Meisner, A. M., Stutz, A. M., et al. 2016, ApJ, 821, 78
Schlafly, E. F., Peek, J. E. G., Finkbeiner, D. P., & Green, G. M. 2017, ApJ,
  838, 36
Schlegel, D. J., Finkbeiner, D. P., & Davis, M. 1998, ApJ, 500, 525
Schmidt, G. D., Cohen, M., & Margon, B. 1980, ApJL, 239, L133
Schödel, R., Najarro, F., Muzic, K., & Eckart, A. 2010, A&A, 511, A18
Schultheis, M., Zasowski, G., Allende Prieto, C., et al. 2014, AJ, 148, 24
Schultz, G. V., & Wiemer, W. 1975, A&A, 43, 133
Schulz, N. S., Corrales, L., & Canizares, C. R. 2016, ApJ, 827, 49
Schutte, W. A., van der Hucht, K. A., Whittet, D. C. B., et al. 1998, A&A,
  337, 261
```

```
Scott, P., Asplund, M., Grevesse, N., Bergemann, M., & Sauval, A. J. 2015a,
   A&A, 573, A26
Scott, P., Grevesse, N., Asplund, M., et al. 2015b, A&A, 573, A25
Serkowski, K. 1971, in IAU Coll. 15: New Directions and New Frontiers in
   Variable Star Research, ed. W. Strohmeier (Paris: IAU), 11
Serkowski, K. 1973, in IAU Symp. 52, Interstellar Dust and Related Topics,
   ed. J. M. Greenberg & H. C. van de Hulst (Dordrecht: Reidel), 145
Serkowski, K., Mathewson, D. S., & Ford, V. L. 1975, ApJ, 196, 261
Seward, F. D., & Smith, R. K. 2013, ApJ, 769, 17
Shalima, P., & Murthy, J. 2004, MNRAS, 352, 1319
Shao, Z., Jiang, B. W., Li, A., et al. 2018, MNRAS, 478, 3467
Shariff, J. A., Ade, P. A. R., Angilè, F. E., et al. 2019, ApJ, 872, 197
Shull, J. M., & van Steenberg, M. E. 1985, ApJ, 294, 599
Siebenmorgen, R., Voshchinnikov, N. V., & Bagnulo, S. 2014, A&A,
   561, A82
Skalidis, R., Panopoulou, G. V., Tassis, K., et al. 2018, A&A, 616, A52
Sloan, G. C., Bregman, J. D., Geballe, T. R., Allamandola, L. J., &
   Woodward, E. 1997, ApJ, 474, 735
Smith, C. H., Aitken, D. K., & Roche, P. F. 1990, MNRAS, 246, 1
Smith, C. H., Wright, C. M., Aitken, D. K., Roche, P. F., & Hough, J. H. 2000,
         AS, 312, 327
Smith, R. K. 2008, ApJ, 681, 343
Smith, R. K., Edgar, R. J., & Shafer, R. A. 2002, ApJ, 581, 562
Smith, T. L., & Witt, A. N. 2002, ApJ, 565, 304
Sneden, C., Gehrz, R. D., Hackwell, J. A., York, D. G., & Snow, T. P. 1978,
   ApJ, 223, 168
Snow, T. P. J., & Cohen, J. G. 1974, ApJ, 194, 313
Sofia, U. J., & Meyer, D. M. 2001, ApJL, 558, L147
Soifer, B. T., Russell, R. W., & Merrill, K. M. 1976, ApJL, 207, L83
Somerville, W. B., Allen, R. G., Carnochan, D. J., et al. 1994, ApJL, 427, L47
Stacey, G. J., Aravena, M., Basu, K., et al. 2018, Proc. SPIE, 10700, 107001M
Stead, J. J., & Hoare, M. G. 2009, MNRAS, 400, 731
Stecher, T. P. 1965, ApJ, 142, 1683
Stecher, T. P., & Donn, B. 1965, ApJ, 142, 1681
Steel, T. M., & Duley, W. W. 1987, ApJ, 315, 337
Sturch, C. 1969, AJ, 74, 82
Szomoru, A., & Guhathakurta, P. 1998, ApJL, 494, L93
Takei, Y., Fujimoto, R., Mitsuda, K., & Onaka, T. 2002, ApJ, 581, 307
Tassis, K., Ramaprakash, A. N., Readhead, A. C. S., et al. 2018, arXiv:1810.
Thompson, G. I., Nandy, K., Morgan, D. H., & Houziaux, L. 1988, MNRAS,
   230, 429
Tielens, A. G. G. M. 2008, ARA&A, 46, 289
Tielens, A. G. G. M., Wooden, D. H., Allamandola, L. J., Bregman, J., &
   Witteborn, F. C. 1996, ApJ, 461, 210
Tokunaga, A. T., Sellgren, K., Smith, R. G., et al. 1991, ApJ, 380, 452
Torres-Dodgen, A. V., Tapia, M., & Carroll, M. 1991, MNRAS, 249, 1
Trumpler, R. J. 1930, PASP, 42, 214
Turcotte, S., & Wimmer-Schweingruber, R. F. 2002, JGRA, 107, 1442
Udalski, A. 2003, ApJ, 590, 284
Vaillancourt, J. E. 2002, ApJS, 142, 53
Vaillancourt, J. E., Dowell, C. D., Hildebrand, R. H., et al. 2008, ApJL,
   679, L25
```

Valencic, L. A., Clayton, G. C., & Gordon, K. D. 2004, ApJ, 616, 912

```
Valencic, L. A., Clayton, G. C., & Gordon, K. D. 2014, ApJ, 793, 66
Valencic, L. A., & Smith, R. K. 2015, ApJ, 809, 66
Valenta, J., Greben, M., Dyakov, S. A., et al. 2019, NatSR, 9, 11214
van Breemen, J. M., Min, M., Chiar, J. E., et al. 2011, A&A, 526, A152
van der Walt, S., Colbert, S. C., & Varoquaux, G. 2011, CSE, 13, 22
Vijh, U. P., Witt, A. N., & Gordon, K. D. 2004, ApJL, 606, L65
Vijh, U. P., Witt, A. N., & Gordon, K. D. 2005, ApJ, 633, 262
Virtanen, P., Gommers, R., Oliphant, T. E., et al. 2020, NatMe, 17, 261
Wada, S., Kaito, C., Kimura, S., Ono, H., & Tokunaga, A. T. 1999, A&A,
Wang, S., & Chen, X. 2019, ApJ, 877, 116
Wang, S., Gao, J., Jiang, B. W., Li, A., & Chen, Y. 2013, ApJ, 773, 30
Westphal, A. J., Butterworth, A. L., Tomsick, J. A., & Gainsforth, Z. 2019,
    pJ, 872, 66
Whiteoak, J. B. 1966, ApJ, 144, 305
Whittet, D. C. B. 1988, MNRAS, 230, 473
Whittet, D. C. B. 2010, ApJ, 710, 1009
Whittet, D. C. B. 2015, ApJ, 811, 110
Whittet, D. C. B., Boogert, A. C. A., Gerakines, P. A., et al. 1997, ApJ,
  490, 729
Whittet, D. C. B., Duley, W. W., & Martin, P. G. 1990, MNRAS, 244, 427
Whittet, D. C. B., Gerakines, P. A., Carkner, A. L., et al. 1994, MNRAS,
  268, 1
Whittet, D. C. B., Martin, P. G., Hough, J. H., et al. 1992, ApJ, 386, 562
Whittet, D. C. B. (ed.) 2003, Dust in the Galactic Environment (Bristol: IOPP)
Wickramasinghe, D. T., & Allen, D. A. 1980, Natur, 287, 518
Wilking, B. A., Lebofsky, M. J., Kemp, J. C., Martin, P. G., & Rieke, G. H.
   1980, ApJ, 235, 905
Wilking, B. A., Lebofsky, M. J., & Rieke, G. H. 1982, AJ, 87, 695
Willner, S. P., Russell, R. W., Puetter, R. C., Soifer, B. T., & Harvey, P. M.
  1979, ApJL, 229, L65
Witt, A. N., Bohlin, R. C., & Stecher, T. P. 1984a, ApJ, 279, 698
Witt, A. N., & Boroson, T. A. 1990, ApJ, 355, 182
Witt, A. N., Friedmann, B. C., & Sasseen, T. P. 1997, ApJ, 481, 809
Witt, A. N., Mandel, S., Sell, P. H., Dixon, T., & Vijh, U. P. 2008, ApJ,
  679, 497
Witt, A. N., Schild, R. E., & Kraiman, J. B. 1984b, ApJ, 281, 708
Witt, A. N., & Vijh, U. P. 2004, in ASP Conf. Ser. 309, Astrophysics of Dust,
  ed. A. N. Witt, G. C. Clayton, & B. T. Draine (San Francisco, CA:
   ASP), 115, arXiv:astro-ph/0309674
Wolff, M. J., Clayton, G. C., Kim, S.-H., Martin, P. G., & Anderson, C. M.
   1997, ApJ, 478, 395
Woolf, N. J., & Ney, E. P. 1969, ApJL, 155, L181
Wright, C. M., Aitken, D. K., Smith, C. H., Roche, P. F., & Laureijs, R. J.
  2002, in Proc. ESO Workshop, The Origin of Stars and Planets: The VLT
   View, ed. J. F. Alves & M. J. McCaughrean (Berlin: Springer), 85
XRISM Science Team 2020, arXiv:2003.04962
Xue, M., Jiang, B. W., Gao, J., et al. 2016, ApJS, 224, 23
York, D. G. 1971, ApJ, 166, 65
Zasowski, G., Majewski, S. R., Indebetouw, R., et al. 2009, ApJ, 707, 510
Zeegers, S. T., Costantini, E., de Vries, C. P., et al. 2017, A&A, 599, A117
Zhang, H., Telesco, C. M., Hoang, T., et al. 2017, ApJ, 844, 6
Zhu, H., Tian, W., Li, A., & Zhang, M. 2017, MNRAS, 471, 3494
Zubko, V., Dwek, E., & Arendt, R. G. 2004, ApJS, 152, 211
```